Posted on 24 Nov 2022 — The copyright holder is the author/funder. All rights reserved. No reuse without permission. — https://doi.org/10.1002/essoar.10512625.1 — This a preprint and has not been peer reviewed. Data may be preliminary.

Global structure of magnetotail reconnection revealed by mining space magnetometer data

Grant K. Stephens[1], Mikhail I. Sitnov[2], Robert S Weigel[3], Drew L. Turner[4], Nikolai A. Tsyganenko[5], Anthony Rogers[6], Kevin J Genestreti[7], and James A. Slavin[8]

[1]Johns Hopkins University Applied Physics Laboratory
[2]JHU/APL
[3]George Mason University
[4]The Johns Hopkins University Applied Physics Laboratory
[5]Saint Petersburg State University
[6]University of New Hampshire
[7]Southwest Research Institute
[8]University of Michigan-Ann Arbor

November 24, 2022

Abstract

Reconnection in the magnetotail occurs along so-called X-lines, where magnetic field lines tear and detach from plasma on microscopic spatial scales (comparable to particle gyroradii). In 2017–2020 the Magnetospheric MultiScale (MMS) mission detected X-lines in the magnetotail enabling their investigation on local scales. However, the global structure and evolution of these X-lines, critical for understanding their formation and total energy conversion mechanisms, remained virtually unknown because of the intrinsically local nature of observations and the extreme sparsity of concurrent data. Here we show that mining a multi-mission archive of space magnetometer data collected over the last 25+ years and then fitting a magnetic field representation modeled using flexible basis-functions, faithfully reconstructs the global pattern of X-lines; 24 of the 26 modeled X-lines match ($B_z=0$ isocontours are within ~2 Earth radii or R_E) or nearly match ($B_z=2$ nT isocontours are within $\sim2 R_E$) the locations of the MMS encountered reconnection sites.

Global structure of magnetotail reconnection revealed by mining space magnetometer data

G. K. Stephens[1], M. I. Sitnov[1], R. S. Weigel[2], D. L. Turner[1], N. A. Tsyganenko[3], A. J. Rogers[4], K. Genestreti[5], and J. A. Slavin[6]

[1]The Johns Hopkins University Applied Physics Laboratory, Laurel, MD 20723, USA
[2]George Mason University, Fairfax, VA 22030, USA
[3]Saint-Petersburg State University, Saint-Petersburg, Russia
[4]University of New Hampshire, Durham, NH, USA
[5]Space Science and Engineering, Southwest Research Institute, Durham, NH, USA
[6]Department of Climate and Space Sciences and Engineering, University of Michigan, Ann Arbor, MI, USA

Key Points:

- Global structure of magnetotail reconnection inferred from data mining matches its locations revealed by in-situ observations
- Reconstructed magnetotail reconnection structures include X- and O-lines, as well as magnetic nulls
- Reconstructed multiscale current sheet structure supports its formation mechanism by quasi-adiabatic ion motions

Corresponding author: Grant K. Stephens, `Grant.Stephens@jhuapl.edu`

Abstract

Reconnection in the magnetotail occurs along so-called X-lines, where magnetic field lines tear and detach from plasma on microscopic spatial scales (comparable to particle gyroradii). In 2017–2020 the Magnetospheric MultiScale (MMS) mission detected X-lines in the magnetotail enabling their investigation on local scales. However, the global structure and evolution of these X-lines, critical for understanding their formation and total energy conversion mechanisms, remained virtually unknown because of the intrinsically local nature of observations and the extreme sparsity of concurrent data. Here we show that mining a multi-mission archive of space magnetometer data collected over the last 25+ years and then fitting a magnetic field representation modeled using flexible basis-functions, faithfully reconstructs the global pattern of X-lines; 24 of the 26 modeled X-lines match ($B_z = 0$ isocontours are within ~ 2 Earth radii or R_E) or nearly match ($B_z = 2$ nT isocontours are within $\sim 2R_E$) the locations of the MMS encountered reconnection sites.

Plain Language Summary

Magnetic reconnection is a fundamental process in plasmas which couples microscopic scales ($\sim$electron to proton gyroradii) to explosive macroscopic phenomena many orders of magnitude larger, such as solar flares and geomagnetic storms/substorms. Reconnection forms along “X-lines”, rifts where oppositely directed magnetic field lines are forced together. In the Earth’s magnetosphere, reconnection has been observed by satellites at isolated locations; however, the large-scale structure of X-lines and their time evolution remains unknown because of the rarity and local nature of observations. Here, ground based measurements of geomagnetic activity and solar wind measurements are used to data-mine 25+ years of magnetometer data from 22 Earth-orbiting satellites, which are then utilized to reconstruct the global magnetic field associated with X-lines in Earth’s magnetosphere. We show that these reconstructions pinpoint the reconnection locations by verifying their consistency with direct spacecraft observations.

1 Introduction

X-lines are one of the most fundamental structures in magnetized plasmas, particularly in space, where they link global or even astronomical scale processes to those on the single particle orbit scale, thereby allowing those microscale processes to shape the universe (Ji et al., 2022). Dungey (1961) suggested that the interaction between Earth’s magnetic dipole and the solar wind causes reconnection of magnetic field lines on both the day and nightsides of Earth’s magnetosphere. The shape of these reconnecting field lines resembles the letter “X” and extends tens of Earth radii ($R_E = 6,371.2$ kilometers) in the dawn-dusk direction thus forming X-lines (Figure 1). An X-line divides space into four sectors. In one pair of opposing sectors, the magnetic field and plasma converge towards the center of the X while in the other pair they are rapidly ejected from it. This reconnection process transforms energy stored in the magnetic field into particle kinetic and thermal energy, making it an efficient energy converter and particle accelerator (Ji et al., 2022). X-lines couple kinetic processes on proton and even electron gyroradius scales ($\lesssim 0.01R_E$) (Torbert et al., 2018) to space weather phenomena on global scales: such as solar flares, coronal mass ejections, and magnetospheric storms and substorms ($\sim 10R_E$) (Camporeale, 2019). This range of scales is so immense that its modeling has become one of the major challenges for nascent exascale computing (Ji et al., 2022).

While the microscale physics of reconnection in the magnetosphere has been studied in detail using recent multi-probe satellite missions (Angelopoulos et al., 2008; Burch et al., 2016; Burch et al., 2016; Torbert et al., 2018), its global structure is difficult to infer from data due to their paucity (rarity and locality): at any moment the huge volume of the magnetosphere ($\gtrsim 10^5 {R_E}^3$) is probed by less than a dozen spacecraft (Sitnov et al., 2019). Understanding the global structure of reconnection is fundamental for determining substorm triggering mechanisms (Sitnov et al., 2019) and the total energy conversion during storms and substorms (Angelopoulos et al., 2013; Angelopoulos et al., 2020). Further, if X-line maps can be constructed from data, these maps could guide

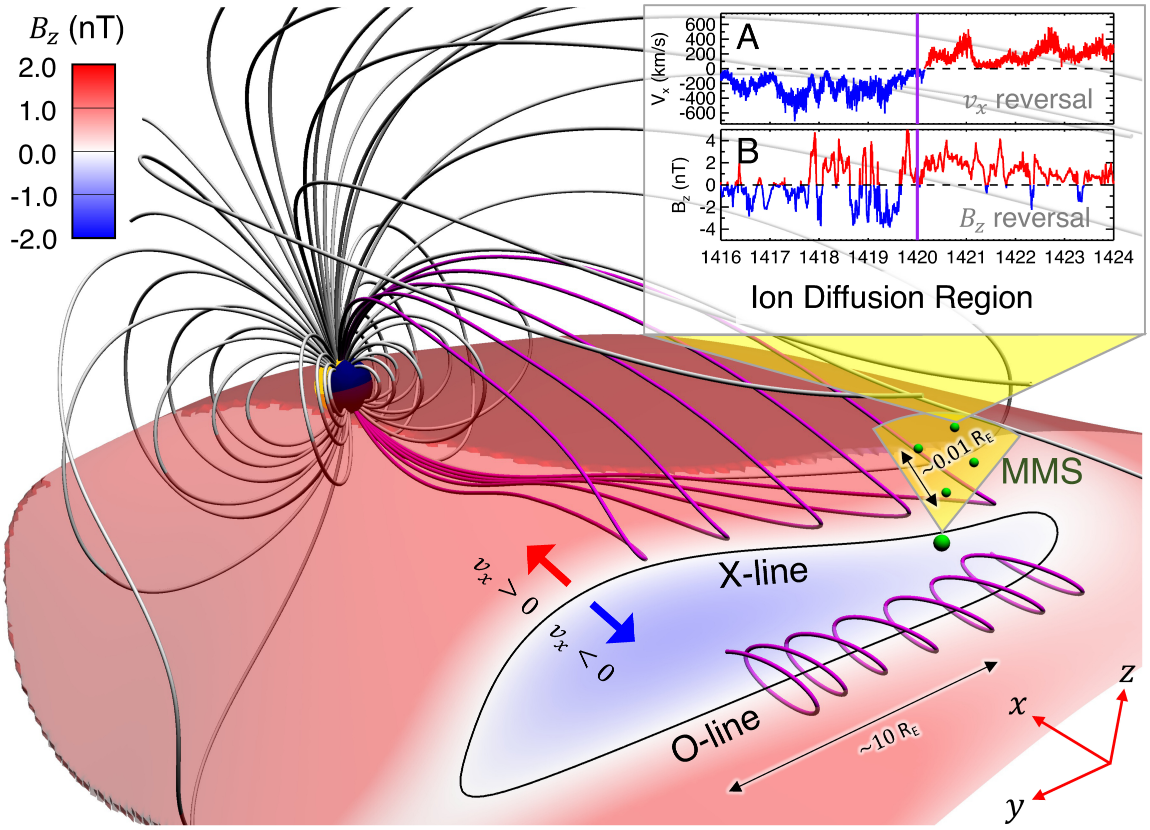

Figure 1. 3D global picture of the magnetosphere and local MMS observations for 5 August 2020 (event Y in Table S2) in GSM coordinates. It shows that the data mining reconstructed X-line hits one of 26 ion diffusion region (IDR) encounters observed by the MMS mission during 2017–2020. It includes selected field lines and the color coded magnetic field distribution, B_z, sampled at the center of the tail current sheet taking into account deformation effects caused by the tilt angle of the Earth's dipole axis as is detailed in the Supporting Information (SI). The $B_z = 0$ isocontour is shown by the black line (the color table is saturated at $|B_z| = 2$ nT to better reveal the isocontour). The inset shows key IDR parameters: (A) the proton bulk flow velocity component v_x and (B) the magnetic field B_z, from the MMS4 probe (the small green spheres show the MMS tetrahedral configuration) whose location is marked by the larger green sphere near the equatorial plane. The purple vertical line marks the reconstruction moment, 5 August 2020, 14:20 UT. The 3D visualizations are constructed using the VisIt visualization tool (Childs et al., 2012).

large-scale magnetohydrodynamic simulations of the magnetosphere by introducing a non-zero resistivity at their locations (Birn et al., 1996).

On the dayside, the X-line location can be readily estimated from the global geometry of the solar wind and Earth's magnetic fields along with other well-defined physical parameters (Fuselier et al., 2011). In contrast, nightside reconnection is much less understood. Here, the solar wind-magnetosphere interaction stretches the dipole field lines in the antisunward direction forming the magnetotail while storing energy in the magnetic field. The release of this stored energy via reconnection is often unsteady and spontaneous. Observations of substorms (Russell & McPherron, 1973; Hones Jr., 1984; Baker et al., 1996; Angelopoulos et al., 2008, 2013) suggest that new X-lines form in the tail at distances of 10–30R_E and that this distance is controlled by the solar wind input (Nagai et al., 2005). However, despite decades of debate and being the target of dedicated satellite missions (Nagai et al., 2005; Angelopoulos et al., 2008; Burch et al., 2016), the factors that determine the emergence, location, size, and shape of nightside X-lines remain a major mystery in heliophysics.

The recent four-probe Magnetospheric MultiScale (MMS) mission (Burch et al., 2016) enabled microscopic analysis of magnetotail reconnection down to electron gyroradius scales (Torbert et al., 2018). During four years of MMS observations, 26 potential X-line encounters were found in the magnetotail (A. J. Rogers et al., 2019; A. Rogers et al., 2021), where explosive reconnection causes substorms (Angelopoulos et al., 2008; Angelopoulos et al., 2020; Sitnov et al., 2019). They were detected in the form of Ion Diffusion Regions (IDRs) characterized by reversals of the North-South component of the magnetic field, B_z, and of the Sun-Earth component of the proton bulk flow velocity, v_x, (Fig. 1 inset).

In this study, the global structure of magnetotail reconnection is derived from a large set of historic satellite magnetometer measurements using an advanced data mining approach. We show that our technique provides evidence justifying the global reconnection structure: the obtained contours delineating B_z reversals pass through most of the micro-scale IDRs discovered by MMS. We further discuss implications of the obtained magnetotail picture to the multiscale structure of its current sheet, and then describe its uncertainty and in-situ validation errors. Throughout this study, vector quantities are represented in the Geocentric Solar Magnetospheric System (GSM).

2 Data Mining Solution of the Data Paucity Problem

The key to solving the data paucity problem lies in the recurrent nature and repeatable pattern of storms and substorms. The storm recurrence time for medium intensity storms is approximately two weeks (Reyes et al., 2021), while it is 2–4 h for periodic substorm (Borovsky & Yakymenko, 2017). This repeatability allows the magnetic field to be reconstructed not only from observations at the moment of interest but also from records identified via mining the space magnetometer archive by searching for other times when the magnetosphere was in a similar global state. The magnetospheric state is characterized using geomagnetic indices (metrics of magnetic activity derived from networks of ground magnetometers) and solar wind conditions. Specifically, the magnetospheric state is defined using a 5-D state-space vector, $\mathbf{G}(t) = (G_1, ..., G_5)$, formed from the geomagnetic storm index (*SMRc*), substorm index (*SML*), their time derivatives, and the solar wind electric field parameter (vB_z^{IMF}; where v is the solar wind speed and B_z^{IMF} is the North-South component of the Interplanetary Magnetic Field, IMF). The *SMR* and *SML* (*SMRc* is a pressure-corrected *SMR* (Tsyganenko et al., 2021)) indices are provided by the SuperMag project (Gjerloev, 2012) and represent variations of the ground-based magnetometer records from low/mid- and high-latitude stations respectively analogous to the *Sym-H* and *AL* indices used before (Sitnov et al., 2008; G. K. Stephens et al., 2019). $G_{1-5}(t)$ are normalized by their standard deviations, smoothed over storm or substorm scales, and sampled at a 5-min cadence, as is detailed in (G. K. Stephens & Sitnov, 2021) and in the Supporting Information (SI). Including the time derivatives of these activity indices allows the data mining (DM) procedure to differentiate between storm and substorms phases as well as capturing memory effects of the magnetosphere as a dynamic system

(Sitnov et al., 2001). The space magnetometer archive contains data from 22 satellites (including the four MMS probes) spanning the years 1995–2020 resulting in 8,649,672 magnetic field measurements after being averaged over 5 and 15 min time windows as is further described in Figure S1 and Table S1 of the SI.

The DM algorithm employed is based on the k-nearest neighbor (kNN) classifier method (Wettschereck et al., 1997; Sitnov et al., 2008). To illustrate the algorithm, assume the magnetic field reconstruction, $\mathbf{B}(t)$, is sought for a query time $t = t^{(q)}$. This corresponds to a particular point in the 5-D state-space, $\mathbf{G}^{(q)} = \mathbf{G}(t^{(q)})$. Surrounding this point will be other points, $\mathbf{G}^{(i)}$, in close proximity to it; i.e., its nearest neighbors (NNs). Distances between points in state-space are computed using the Euclidean metric: $R_i = |\mathbf{G}^{(i)} - \mathbf{G}^{(q)}|$. Time-adjacent NNs form intervals in time that identify a subset of the magnetometer database used to fit the analytical formulation of the magnetic field, yielding $\mathbf{B}(t^{(q)})$. The specific choice of the number of NNs to use in the reconstruction, k_{NN}, is dictated by a balance between over- and under-fitting. G. K. Stephens and Sitnov (2021) found the optimal number to be $k_{NN} = 32,000$ for tail reconstructions of substorms, corresponding to $\sim 1\%$ of the total database. The resulting subset is composed of a very small number ($\sim$ 1–10) of real (from the event of interest) but many ($\sim 10^5$) virtual (from other events) satellites.

The large number of virtual points enables new magnetic field architectures (Tsyganenko & Sitnov, 2007; G. K. Stephens et al., 2019), which differ from classical empirical models with custom-tailored modules (e.g., Tsyganenko & Sitnov, 2005) by utilizing regular basis function expansions for the major magnetospheric current systems, to be used for the reconstructions. In particular, all near-equatorial currents are approximated by two expansions representing general current distributions of thick and thin current sheets with different thickness parameters D and D_{TCS}. The latter accounts for the formation of ion-scale thin current sheets (TCS) prior to substorm onset (V. Sergeev et al., 2011), as is further detailed below. The independence of the current sheet expansions is provided by the constraint $D_{TCS} < D$. To improve the reconstructions, while fitting the magnetic field model with the NN subset, the spacecraft data were additionally weighted: in the real space (to mitigate the inhomogeneity of their radial distribution (Tsyganenko & Sitnov, 2007)) and in the state-space (to reduce the uncertainty and bias toward weaker activity regions (G. K. Stephens & Sitnov, 2021)) as it is further detailed in the SI.

The resulting DM reconstruction of the magnetic field during the early expansion phase of the 5 August 2020 substorm (Figure 1) reveals the formation of an X-line at $r \approx 23R_E$ in the tail. This data-derived image of the X-line resembles sketches of solar flare arcades (e.g., Shiota et al., 2005) but with a fundamental advantage that it is backed by a quantitative description. The X-line appears on the dusk flank of the tail illustrated as the earthward part of the $B_z = 0$ isocontour in the equatorial plane (black line). It also corresponds to an earthward edge of a relatively long ($25R_E$) spiral structure, shown by the sample field lines that encircle the tailward part of the $B_z = 0$ isocontour and form a magnetic O-line. The large green sphere in Figure 1 indicates the location of the MMS satellites at this moment with the inset, which shows the observed B_z and v_x, demonstrating it was one of the fortuitous IDR encounters.

3 Ion Diffusion Regions

The main goal of the MMS mission (Burch et al., 2016) was the detection and investigation of reconnection regions in the magnetosphere and its boundary. That goal was relatively easy to achieve at the magnetopause because of its regular structure (Fuselier et al., 2011) and in the magnetosheath due to multiple reconnection sites in its turbulent plasma volume (Phan et al., 2018). By contrast, only a handful of fortunate X-line encounters were detected/investigated in the magnetotail (Torbert et al., 2018; Chen et al., 2019). In this regard, the proposed DM reconstructions offer an attractive opportunity to explore the dynamics of magnetotail topology on a global scale, and its fidelity can be demonstrated by comparing our results with MMS observations. Magnetic reconnection can be directly observed if and when a spacecraft fortuitously flies through an Ion Diffusion Region (IDR), as shown in Figure 1. A recent systematic survey of MMS plasma and

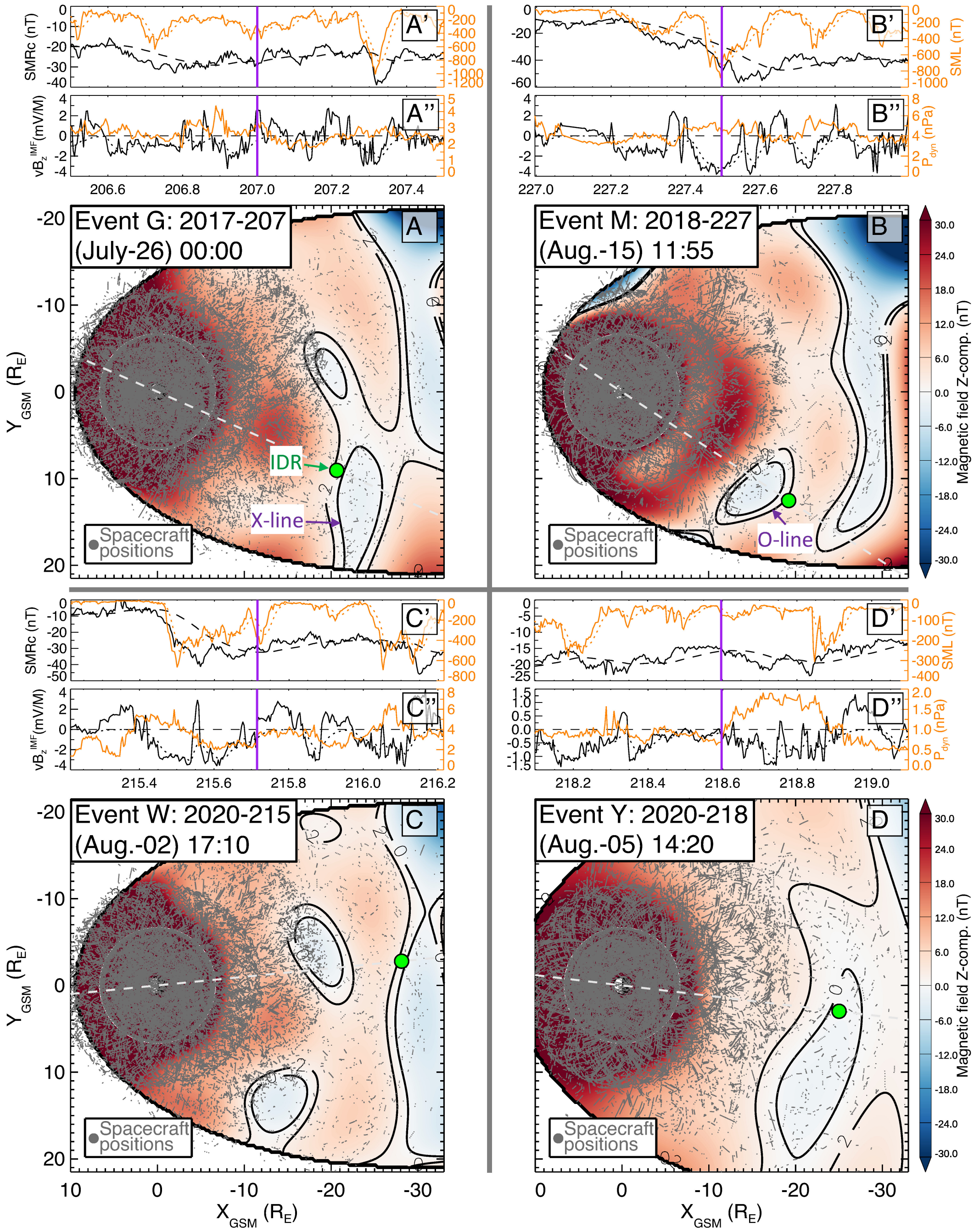

Figure 2. IDRs and the equatorial magnetic field landscape. (A–D) Color-coded distributions of the equatorial magnetic field, B_z, with $B_z = 0$ and 2 nT isocontours (black lines), big green dots pointing to the IDRs, and gray dots showing the spacecraft positions for the NN subsets used in the DM method for four IDR events, G, M, W and Y. Panels on top of each equatorial B_z distribution show the global context of the considered events in terms of (A'–D') the storm and substorm indices *SMRc* (black), *SML* (orange), and (A''–D'') the solar wind/IMF parameters vB_z^{IMF} (black) and P_{dyn} (orange) with the purple vertical line marking the event time.

field data in 2017 (A. J. Rogers et al., 2019) identified 12 such magnetotail IDRs, defined as correlated reversals of the proton bulk flow velocity, v_x, and the North-South magnetic field, B_z, as shown in the Figure 1 inset, along with additional Hall magnetic and electric field signatures. That analysis was later extended to 2018–2020 for a total of 26 IDR events (A. Rogers et al., 2021) labeled here A–Z, "IDR alphabet", listed in Table S2 in the SI.

Figure 1 shows that the DM reconstruction correctly identifies one of the IDR regions, namely event Y (5 August 2020 14:20 UT), whose v_x and B_z reversals are shown in the inset. The projection of the magnetic field at the center of the tail current sheet into the equatorial plane is displayed in Figure 2D showing that the $B_z = 0$ contour passes within $\sim 1R_E$ of the IDR observed by MMS. This success is remarkable given that only $\sim 0.03\%$ of the measurements used to reconstruct the magnetic field were taken from this event, with the other 99.97% coming from other similar events identified using the above described DM approach. Below we show that similar $B_z = 0$ contours pass through most of the microscale IDRs discovered by MMS.

3.1 Reconstructed X- and O-lines in the Equatorial Plane

The reconstructions of 3 other events (G, M, W) presented in Figure 2 also show the $B_z = 0$ contours pass within $\sim 1R_E$ of the observed IDRs (the exact distances are provided in Table S2). Closer examination shows that only events G, W, and Y are X-lines, whereas event M corresponds to an O-line. Indeed, since the microscale formation of the MMS tetrahedron cannot determine X-line motions using timing analysis, (e.g., Eastwood et al., 2010), or by framing the X-lines by being tailward and earthward of them (Angelopoulos et al., 2008), it cannot distinguish whether they are X- or O-lines.

The equatorial X-line reconstructions for the remaining 22 IDR events are provided in Figs. S3–S8. They reveal that the DM approach hits 16 of the 26 IDRs (Figs. 2 and S3–S5), that is, the $B_z = 0$ contours pass within $\lesssim 2R_E$ of the IDRs, which includes 11 X-lines and 5 O-lines. Another 8 events are near hits, that is, the IDRs are located within $\lesssim 2R_E$ from $B_z = 2$ nT contours (Figs. S6 and S7). Only in 2 events (B, F) do the reconstructed $B_z = 0$ contours miss their IDR targets (Figure S8); however, both events have a plausible explanation. Event B occurs during weak magnetospheric activity ($SML \approx 0$) with effectively no solar wind/IMF input ($vB_z^{IMF} > 0$) while event F takes place during the middle of a several hours long gap in solar wind and IMF data (they are interpolated in the reconstruction).

3.2 Reconnection Features in the Meridional Planes

The corresponding meridional slices through the planes containing the IDRs of the Figure 2 events (G, M, W, Y) are shown in Figure 3, illustrating the magnetic topology and distributions of electric currents, while the remainder of the IDR alphabet (Figures S3–S8) is shown in Figures S9–S14. The figures clarify that the observed $B_z = 0$ contours indeed represent X- and O-lines similar to the 3D magnetotail field geometry shown in Figure 1. They also confirm the quasi-2-D nature of reconnection apparently imposed by the North-South symmetry of the magnetotail (e.g., Tsyganenko & Fairfield, 2004) which is drastically different from the inherently 3-D reconnection processes in the solar corona (Liu et al., 2016) and rapidly rotating planets (Griton et al., 2018).

These meridional distributions resemble empirical visualizations of reconnection in laboratory plasmas, which became possible due to their large number of real probes (up to 200) and additional symmetry constraints, such as the cylindrical symmetry imposed by the toroidal-shaped flux cores in the PPPL Magnetic Reconnection Experiment (MRX) (Ji et al., 2022). Still, in contrast to MRX, magnetotail reconnection is only quasi 2-D due to the finite length of the X-line forming a closed loop with the O-line, as well as the explicit 3-D effects, such as null-points (e.g., Greene, 1988; Ji et al., 2022). Null-points in the tail were indeed inferred from the four-probe Cluster observations (Xiao et al., 2006). An example of the null-point pair seen in our DM reconstruction of event Y is presented in Figure S15. Additional deviations from the simple 2-D

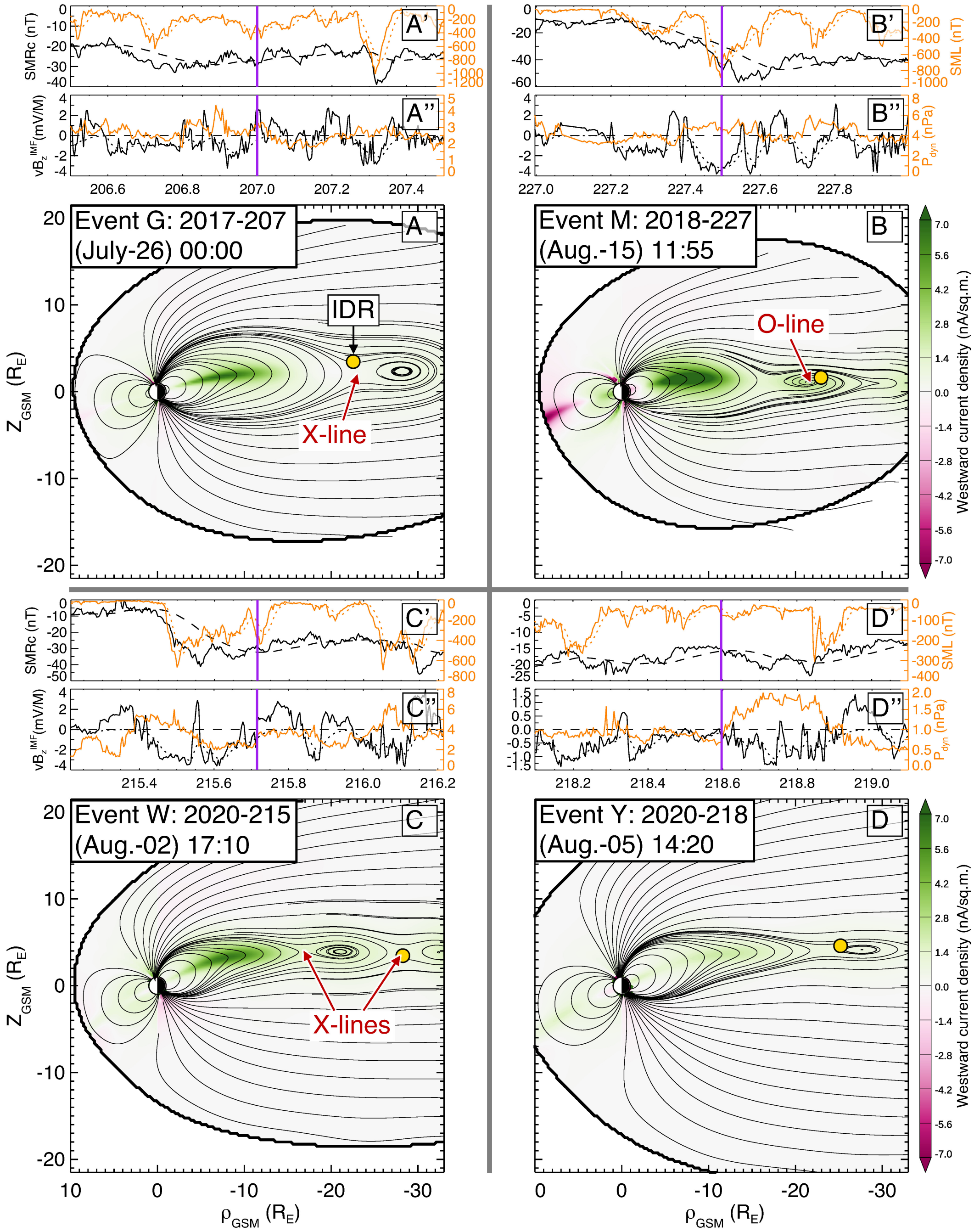

Figure 3. IDRs against the meridional current and magnetic field distributions. (A–D) Color-coded distribution of the electric current perpendicular (westward positive) to the meridional plane, which contains the corresponding IDR (white dashed lines in Figure 2), for four events shown in Figure 2 with the similar format for global parameters (A'–D') and (A''–D'') on top of each distribution. The IDRs are shown here by big orange dots. Thin and thick lines show the magnetic field lines and the magnetospheric boundary (magnetopause).

picture could be due to a strong IMF B_y (e.g., Cowley, 1981) or North-South oscillations of the tail current sheet that resemble a flapping flag (e.g., V. A. Sergeev et al., 2006; Sitnov et al., 2019).

Note that in the present reconstructions the original multiscale tail model (G. K. Stephens et al., 2019) with the embedded TCS structure has been further generalized to verify the possible physical mechanisms of the TCS formation. It can be explained, (e.g., Sitnov et al., 2006), by figure-eight like Speiser (1965) proton orbits. If this is the case, the parameter D_{TCS} of the magnetic field model should depend on the distance ρ from the Earth because the Speiser orbit size, ρ_{Si}, is inversely proportional to the magnetic field outside the sheet, B_L, which itself depends on ρ (Wang et al., 2004). To take this effect into account the magnetic field architecture was further generalized using the approximation $D_{TCS}(\rho) = [D_*^{-1} + \alpha \exp(-\beta\rho)]^{-1}$ with free parameters α, β and D_* to be inferred from data. The fitting details provided in Figure S2 suggest that the scaling $D_{TCS} \propto B_L^{-1} \propto \rho_{Si}$ does indeed take place, which supports the theoretical mechanism of the TCS formation related to the Speiser orbits.

4 Validation and Uncertainty Quantification

An example of in-situ validation of this global reconstruction, rarely possible because of the data paucity, is shown in Figs. 4A–4D for the MMS magnetic field observations of the tail during event Y. It reveals relatively large deviations in the magnetic field components $B_{x,y}$ parallel to the current plane (Figs. 4A, 4B). They are likely caused by the flapping North-South motions of the current sheet as a whole (V. A. Sergeev et al., 2006) that were found in MMS observations as well (Farrugia et al., 2021). These motions are spontaneous and may appear in different phases of activity, so it is not surprising that they are not captured by the DM reconstructions. At the same time, the B_z magnetic field is reproduced even better than it appears in observations after 5-min averages (compare the black line in Figure 4C with the inset in Figure 1). Thus, hitting 24 out of 26 IDRs, achieved in this study, shows (i) how to overcome the curse of data paucity for in-situ data and (ii) presents solid evidence that not only validates our DM reconstructions, but also helps understand the reconnection mechanisms and its consequences.

The fidelity of the present reconstructions can also be seen from the uncertainty analysis presented in Figs. 4E–I. It compares 5 original binning parameters of the magnetosphere with their means and standard deviations over the NN bins. The closeness of means to the original parameters G_{1-5} and small relative values of deviations suggest that the selected NNs closely follow the magnetospheric dynamics, especially on substorm scales (Figs. 4G–4H).

5 Conclusions

This picture of the 2017–2020 MMS IDR alphabet suggests that, in spite of the extreme paucity of in-situ observations, DM successfully reconstructs the overall structure of magnetotail X- and O-lines because they are strongly self-organized on the global scale. The X-lines vary in length from 5 to $40R_E$, with the shorter ones forming inside of $\sim 20R_E$ while the longer ones, $\sim 40R_E$, appear beyond $25R_E$. The concurrent appearance of such near-Earth and midtail X-lines is consistent with the original conjectures regarding new X-line formation during substorms (Hones Jr., 1984). It also explains the detection of X-lines as discrete points in radial distance in remote sensing (Angelopoulos et al., 2013, Fig. 3C) as well as the stepwise retreat of magnetic reconnection regions suggested by their auroral manifestations and confirmed by in-situ observations (Ieda et al., 2016). The persistent formation of X-lines near $30R_E$ has also been confirmed by the statistical analysis of the travelling compression regions (Imber et al., 2011). The success of our X-line reconstruction indicates that year after year, the spatial/temporal patterns of storms and substorms in the Earth's magnetotail are highly recurrent and hence reproducible with historic data, while magnetic reconnection controls the global state of the magnetosphere reflected in its activity indices, their trends, and the solar wind energy input.

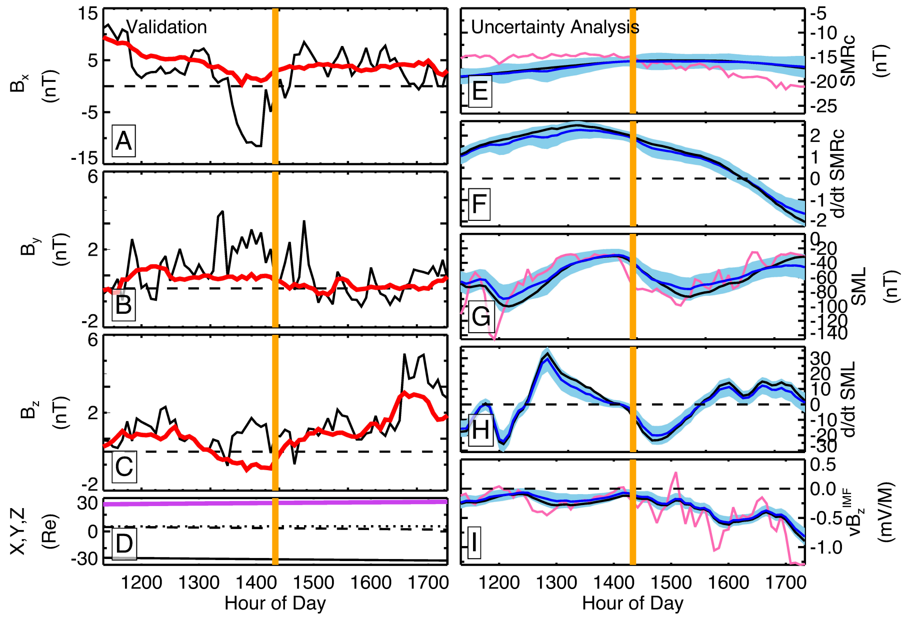

Figure 4. Validation and uncertainty analysis for event Y. (A)–(C) The 5-min averaged GSM magnetic field components (black lines) and their DM reconstructions (red lines). (D) MMS ephemeris (in GSM) X (solid line), Y (dashed line), Z (dash-dotted line) and the radial distance (pink line). (E)–(I) The storm/substorm state binning parameters $\langle SMRc|$, $D\langle SMRc|/Dt$, $\langle SML|$, $D\langle SML|/Dt$, and $\langle vB_s^{IMF}|$ as described in the SI, shown by black lines as compared to their means over the NNs (blue lines). The light blue shading shows the standard deviations $\pm 1\sigma$ of the NNs. Pink lines in Figs. 4E, 4G, and 4I show the original 5-min OMNI data for the parameters *SMRc* (pressure-corrected *SMR* (Tsyganenko et al., 2021)), *SML*, and vB_z^{IMF}. Yellow bars show the moment of the spatial reconstruction 5 August 2020, 14:20 UT shown in Figs. 1, 2D and 3D.

6 Open Research

The data used in the paper are archived on Zenodo (G. Stephens et al., 2022). For each of the 26 IDR events, files are included that detail: time intervals identified using the nearest-neighbor search and the resulting subset of magnetometer data and their associated weights, files containing the fit set of coefficients and parameters for the model, and the digital model output data that were used in constructing the figures. The compiled magnetometer database used in this study is available on the SPDF website (Korth et al., 2018). This study extended this database with the addition of MMS magnetometer data which has also been included in the Zenodo archive. The SMR and SML indices obtained from the SuperMAG web page are also included in the Zenodo archive. The data describing the solar wind conditions were taken from the 5-min OMNI data (Papitashvili & King, 2020).

Acknowledgments

The authors acknowledge useful discussions with G. Clark, R. Nakamura, S. Sharma, H. Spence, V. Titov, J. Vandegriff, D. Vassiliadis, and J. Zhang. They thank the SuperMag team and their collaborators, which provided the global indices of the storm and substorm activity. They also thank the teams who created and provided Geotail, Polar, IMP 8, Cluster, THEMIS, Van Allen Probes, MMS and GOES data obtained via NSSDC CDAWeb online facility, as well as Wind and ACE solar wind/IMF data that went into the production of the OMNI data obtained via NASA/GSFC's Space Physics Data Facility's OMNIWeb service. This work was funded by NASA grants 80NSSC19K0074, 80NSSC20K1271, 80NSSC20K1787, as well as NSF grants AGS-1702147 and AGS-1744269. N. A. Tsyganenko acknowledges support of the RFBR grant 20-05-00218.

References

Angelopoulos, V., Artemyev, A., Phan, T. D., & Miyashita, Y. (2020, January). Near-Earth magnetotail reconnection powers space storms. *Nature Physics*, *16*(3), 317-321. doi: 10.1038/s41567-019-0749-4

Angelopoulos, V., McFadden, J. P., Larson, D., Carlson, C. W., Mende, S. B., Frey, H., ... Kepko, L. (2008). Tail reconnection triggering substorm onset. *Science*, *321*(5891), 931–935. Retrieved from `https://science.sciencemag.org/content/321/5891/931` doi: 10.1126/science.1160495

Angelopoulos, V., Runov, A., Zhou, X.-Z., Turner, D. L., Kiehas, S. A., Li, S.-S., & Shinohara, I. (2013). Electromagnetic energy conversion at reconnection fronts. *Science*, *341*(6153), 1478–1482. Retrieved from `https://science.sciencemag.org/content/341/6153/1478` doi: 10.1126/science.1236992

Baker, D. N., Pulkkinen, T. I., Angelopoulos, V., Baumjohann, W., & McPherron, R. L. (1996). Neutral line model of substorms: Past results and present view. *Journal of Geophysical Research: Space Physics*, *101*(A6), 12975-13010. doi: 10.1029/95JA03753

Birn, J., Hesse, M., & Schindler, K. (1996). Mhd simulations of magnetotail dynamics. *Journal of Geophysical Research: Space Physics*, *101*(A6), 12939-12954. doi: https://doi.org/10.1029/96JA00611

Borovsky, J. E., & Yakymenko, K. (2017). Substorm occurrence rates, substorm recurrence times, and solar wind structure. *Journal of Geophysical Research: Space Physics*, *122*(3), 2973-2998. doi: https://doi.org/10.1002/2016JA023625

Burch, J. L., Moore, T. E., Torbert, R. B., & Giles, B. L. (2016, March). Magnetospheric Multiscale Overview and Science Objectives. *Space Science Reviews*, *199*(1-4), 5-21. doi: 10.1007/s11214-015-0164-9

Burch, J. L., Torbert, R. B., Phan, T. D., Chen, L.-J., Moore, T. E., Ergun, R. E., ... Chandler, M. (2016). Electron-scale measurements of magnetic reconnection in space. *Science*, *352*(6290), 10.1126/science.aaf2939. Retrieved from `https://science.sciencemag.org/content/352/6290/aaf2939` doi: 10.1126/science.aaf2939

Camporeale, E. (2019). The challenge of machine learning in space weather: Nowcasting and forecasting. *Space Weather*, *17*(8), 1166-1207. doi: https://doi.org/10.1029/2018SW002061

Chen, L.-J., Wang, S., Hesse, M., Ergun, R. E., Moore, T., Giles, B., … Lindqvist, P.-A. (2019). Electron diffusion regions in magnetotail reconnection under varying guide fields. *Geophysical Research Letters*, *46*(12), 6230-6238. doi: https://doi.org/10.1029/2019GL082393

Childs, H., Brugger, E., Whitlock, B., Meredith, J., Ahern, S., Pugmire, D., … Navrátil, P. (2012, October). Visit: An end-user tool for visualizing and analyzing very large data. In *High performance visualization–enabling extreme-scale scientific insight* (p. 357-372). doi: 10.1201/b12985

Cowley, S. (1981). Magnetospheric asymmetries associated with the y-component of the IMF. *Planetary and Space Science*, *29*(1), 79-96. Retrieved from `https://www.sciencedirect.com/science/article/pii/0032063381901410` doi: https://doi.org/10.1016/0032-0633(81)90141-0

Dungey, J. W. (1961). Interplanetary magnetic field and the auroral zones. *Phys. Rev. Lett.*, *6*, 47–48. Retrieved from `https://link.aps.org/doi/10.1103/PhysRevLett.6.47` doi: 10.1103/PhysRevLett.6.47

Eastwood, J. P., Phan, T. D., Øieroset, M., & Shay, M. A. (2010). Average properties of the magnetic reconnection ion diffusion region in the earth's magnetotail: The 2001-2005 Cluster observations and comparison with simulations. *Journal of Geophysical Research: Space Physics*, *115*(A8), https://doi.org/10.1029/2009JA014962. doi: https://doi.org/10.1029/2009JA014962

Farrugia, C. J., Rogers, A. J., Torbert, R. B., Genestreti, K. J., Nakamura, T. K. M., Lavraud, B., … Dors, I. (2021). An encounter with the ion and electron diffusion regions at a flapping and twisted tail current sheet. *Journal of Geophysical Research: Space Physics*, *126*(3), e2020JA028903. doi: https://doi.org/10.1029/2020JA028903

Fuselier, S. A., Trattner, K. J., & Petrinec, S. M. (2011). Antiparallel and component reconnection at the dayside magnetopause. *Journal of Geophysical Research: Space Physics*, *116*(A10), https://doi.org/10.1029/2011JA016888. Retrieved from `https://agupubs.onlinelibrary.wiley.com/doi/abs/10.1029/2011JA016888` doi: https://doi.org/10.1029/2011JA016888

Gjerloev, J. W. (2012). The supermag data processing technique. *Journal of Geophysical Research: Space Physics*, *117*(A9), https://doi.org/10.1029/2012JA017683. doi: https://doi.org/10.1029/2012JA017683

Greene, J. M. (1988). Geometrical properties of three-dimensional reconnecting magnetic fields with nulls. *Journal of Geophysical Research: Space Physics*, *93*(A8), 8583-8590. doi: https://doi.org/10.1029/JA093iA08p08583

Griton, L., Pantellini, F., & Meliani, Z. (2018). Three-dimensional magnetohydrodynamic simulations of the solar wind interaction with a hyperfast-rotating uranus. *Journal of Geophysical Research: Space Physics*, *123*(7), 5394-5406. doi: https://doi.org/10.1029/2018JA025331

Hones Jr., E. W. (1984). Magnetic reconnection in space and laboratory plasmas. In (p. 178-184). American Geophysical Union. doi: https://doi.org/10.1029/GM030p0178

Ieda, A., Nishimura, Y., Miyashita, Y., Angelopoulos, V., Runov, A., Nagai, T., … Machida, S. (2016). Stepwise tailward retreat of magnetic reconnection: Themis observations of an auroral substorm. *Journal of Geophysical Research: Space Physics*, *121*(5), 4548-4568. doi: https://doi.org/10.1002/2015JA022244

Imber, S. M., Slavin, J. A., Auster, H. U., & Angelopoulos, V. (2011). A themis survey of flux ropes and traveling compression regions: Location of the near-earth reconnection site during solar minimum. *Journal of Geophysical Research: Space Physics*, *116*(A2), https://doi.org/10.1029/2010JA016026. doi: https://doi.org/10.1029/2010JA016026

Ji, H., Daughton, W., Jara-Almonte, J., Le, A., Stanier, A., & Yoo, J. (2022). Magnetic reconnection in the era of exascale computing and multiscale experiments. *Nature Re-*

views Physics, *4*, 263–282. doi: 10.1038/s42254-021-00419-x

Korth, H., Sitnov, M., & Stephens, G. (2018). *Magnetic field modeling database description final* [dataset]. NASA Space Physics Data Facility. Retrieved from https://spdf.gsfc.nasa.gov/pub/data/aaa_special-purpose-datasets/empirical-magnetic-field-modeling-database-with-TS07D-coefficients/

Liu, R., Kliem, B., Titov, V. S., Chen, J., Wang, Y., Wang, H., ... Wiegelmann, T. (2016, feb). STRUCTURE, STABILITY, AND EVOLUTION OF MAGNETIC FLUX ROPES FROM THE PERSPECTIVE OF MAGNETIC TWIST. *The Astrophysical Journal*, *818*(2), 148. Retrieved from https://doi.org/10.3847/0004-637x/818/2/148 doi: 10.3847/0004-637x/818/2/148

Nagai, T., Fujimoto, M., Nakamura, R., Baumjohann, W., Ieda, A., Shinohara, I., ... Mukai, T. (2005). Solar wind control of the radial distance of the magnetic reconnection site in the magnetotail. *Journal of Geophysical Research: Space Physics*, *110*(A9), https://doi.org/10.1029/2005JA011207. Retrieved from https://agupubs.onlinelibrary.wiley.com/doi/abs/10.1029/2005JA011207 doi: https://doi.org/10.1029/2005JA011207

Papitashvili, N. E., & King, J. H. (2020). *Omni 5-min data* [dataset]. NASA Space Physics Data Facility. Retrieved from https://www.unavco.org/data/doi/10.7283/633E-1497 doi: 10.48322/gbpg-5r77

Phan, T. D., Eastwood, J. P., Shay, M. A., Drake, J. F., Sonnerup, B. U. Ö., Fujimoto, M., ... Magnes, W. (2018, May 01). Electron magnetic reconnection without ion coupling in Earth's turbulent magnetosheath. *Nature*, *557*(7704), 202-206. Retrieved from https://doi.org/10.1038/s41586-018-0091-5 doi: 10.1038/s41586-018-0091-5

Reyes, P. I., Pinto, V. A., & Moya, P. S. (2021). Geomagnetic storm occurrence and their relation with solar cycle phases. *Space Weather*, *19*(9), e2021SW002766. doi: https://doi.org/10.1029/2021SW002766

Rogers, A., Farrugia, C. J., Torbert, R. B., & Rogers, T. J. (2021). Applying magnetic curvature to to MMS data to identify thin current sheets relative to tail reconnection. *Earth and Space Science Open Archive*, 12. doi: 10.1002/essoar.10509282.1

Rogers, A. J., Farrugia, C. J., & Torbert, R. B. (2019). Numerical algorithm for detecting ion diffusion regions in the geomagnetic tail with applications to mms tail season 1 may to 30 september 2017. *Journal of Geophysical Research: Space Physics*, *124*(8), 6487-6503. Retrieved from https://agupubs.onlinelibrary.wiley.com/doi/abs/10.1029/2018JA026429 doi: https://doi.org/10.1029/2018JA026429

Russell, C. T., & McPherron, R. L. (1973, Nov 01). The magnetotail and substorms. *Space Science Reviews*, *15*(2), 205-266. Retrieved from https://doi.org/10.1007/BF00169321 doi: 10.1007/BF00169321

Sergeev, V., Angelopoulos, V., Kubyshkina, M., Donovan, E., Zhou, X.-Z., Runov, A., ... Nakamura, R. (2011). Substorm growth and expansion onset as observed with ideal ground-spacecraft themis coverage. *Journal of Geophysical Research: Space Physics*, *116*(A5), https://doi.org/10.1029/2010JA015689. doi: https://doi.org/10.1029/2010JA015689

Sergeev, V. A., Sormakov, D. A., Apatenkov, S. V., Baumjohann, W., Nakamura, R., Runov, A. V., ... Nagai, T. (2006). Survey of large-amplitude flapping motions in the midtail current sheet. *Annales Geophysicae*, *24*(7), 2015–2024. Retrieved from https://angeo.copernicus.org/articles/24/2015/2006/ doi: 10.5194/angeo-24-2015-2006

Shiota, D., Isobe, H., Chen, P. F., Yamamoto, T. T., Sakajiri, T., & Shibata, K. (2005, nov). Self-consistent magnetohydrodynamic modeling of a coronal mass ejection, coronal dimming, and a giant cusp-shaped arcade formation. *The Astrophysical Journal*, *634*(1), 663–678. Retrieved from https://doi.org/10.1086/496943 doi: 10.1086/496943

Sitnov, M., Birn, J., Ferdousi, B., Gordeev, E., Khotyaintsev, Y., Merkin, V., ... Zhou, X. (2019, June). Explosive Magnetotail Activity. *Space Science Reviews*, *215*(4), 31. doi:

10.1007/s11214-019-0599-5
Sitnov, M. I., Sharma, A. S., Papadopoulos, K., & Vassiliadis, D. (2001, Dec). Modeling substorm dynamics of the magnetosphere: From self-organization and self-organized criticality to nonequilibrium phase transitions. *Phys. Rev. E*, *65*, 016116. Retrieved from `https://link.aps.org/doi/10.1103/PhysRevE.65.016116` doi: 10.1103/PhysRevE.65.016116
Sitnov, M. I., Stephens, G. K., Tsyganenko, N. A., Miyashita, Y., Merkin, V. G., Motoba, T., … Genestreti, K. J. (2019). Signatures of nonideal plasma evolution during substorms obtained by mining multimission magnetometer data. *Journal of Geophysical Research: Space Physics*, *124*(11), 8427-8456. doi: 10.1029/2019JA027037
Sitnov, M. I., Swisdak, M., Guzdar, P. N., & Runov, A. (2006). Structure and dynamics of a new class of thin current sheets. *Journal of Geophysical Research: Space Physics*, *111*(A8), https://doi.org/10.1029/2005JA011517. doi: https://doi.org/10.1029/2005JA011517
Sitnov, M. I., Tsyganenko, N. A., Ukhorskiy, A. Y., & Brandt, P. C. (2008). Dynamical data-based modeling of the storm-time geomagnetic field with enhanced spatial resolution. *Journal of Geophysical Research: Space Physics*, *113*(A7), 10.1029/2007JA013003. doi: 10.1029/2007JA013003
Speiser, T. W. (1965). Particle trajectories in model current sheets: 1. analytical solutions. *Journal of Geophysical Research (1896-1977)*, *70*(17), 4219-4226. doi: https://doi.org/10.1029/JZ070i017p04219
Stephens, G., Sitnov, M., Weigel, R., Turner, D., Tsyganenko, N., Rogers, A., … Slavin, J. (2022). *Global structure of magnetotail reconnection revealed by mining space magnetometer data* [dataset]. Zenodo. Retrieved from `https://doi.org/10.5281/zenodo.6862829` doi: 10.5281/zenodo.6862829
Stephens, G. K., & Sitnov, M. I. (2021). Concurrent empirical magnetic reconstruction of storm and substorm spatial scales using data mining and virtual spacecraft. *Frontiers in Physics*, *9*, 210. Retrieved from `https://www.frontiersin.org/article/10.3389/fphy.2021.653111` doi: 10.3389/fphy.2021.653111
Stephens, G. K., Sitnov, M. I., Korth, H., Tsyganenko, N. A., Ohtani, S., Gkioulidou, M., & Ukhorskiy, A. Y. (2019). Global empirical picture of magnetospheric substorms inferred from multimission magnetometer data. *Journal of Geophysical Research: Space Physics*, *124*(2), 1085-1110. Retrieved from `https://agupubs.onlinelibrary.wiley.com/doi/abs/10.1029/2018JA025843` doi: 10.1029/2018JA025843
Torbert, R. B., Burch, J. L., Phan, T. D., Hesse, M., Argall, M. R., Shuster, J., … Saito, Y. (2018). Electron-scale dynamics of the diffusion region during symmetric magnetic reconnection in space. *Science*, *362*(6421), 1391–1395. Retrieved from `https://science.sciencemag.org/content/362/6421/1391` doi: 10.1126/science.aat2998
Tsyganenko, N. A., Andreeva, V. A., Sitnov, M. I., Stephens, G. K., Gjerloev, J. W., Chu, X., & Troshichev, O. A. (2021). Reconstructing substorms via historical data mining: Is it really feasible? *Journal of Geophysical Research: Space Physics*, *126*(10), e2021JA029604. doi: https://doi.org/10.1029/2021JA029604
Tsyganenko, N. A., & Fairfield, D. H. (2004). Global shape of the magnetotail current sheet as derived from geotail and polar data. *Journal of Geophysical Research: Space Physics*, *109*(A3), https://doi.org/10.1029/2003JA010062. doi: https://doi.org/10.1029/2003JA010062
Tsyganenko, N. A., & Sitnov, M. I. (2005). Modeling the dynamics of the inner magnetosphere during strong geomagnetic storms. *Journal of Geophysical Research: Space Physics*, *110*(A3). doi: 10.1029/2004JA010798
Tsyganenko, N. A., & Sitnov, M. I. (2007). Magnetospheric configurations from a high-resolution data-based magnetic field model. *Journal of Geophysical Research: Space Physics*, *112*(A6), 10.1029/2007JA012260. doi: 10.1029/2007JA012260
Wang, C.-P., Lyons, L. R., Nagai, T., & Samson, J. C. (2004). Midnight radial profiles of the

quiet and growth-phase plasma sheet: The geotail observations. *Journal of Geophysical Research: Space Physics*, *109*(A12), https://doi.org/10.1029/2004JA010590. doi: https://doi.org/10.1029/2004JA010590

Wettschereck, D., Aha, D. W., & Mohri, T. (1997, Feb 01). A review and empirical evaluation of feature weighting methods for a class of lazy learning algorithms. *Artificial Intelligence Review*, *11*(1), 273-314. Retrieved from `https://doi.org/10.1023/A:1006593614256` doi: 10.1023/A:1006593614256

Xiao, C. J., Wang, X. G., Pu, Z. Y., Zhao, H., Wang, J. X., Ma, Z. W., ... Escoubet, C. P. (2006, Jul 01). In situ evidence for the structure of the magnetic null in a 3d reconnection event in the earth's magnetotail. *Nature Physics*, *2*(7), 478-483. Retrieved from `https://doi.org/10.1038/nphys342` doi: 10.1038/nphys342

Supporting Information for "Global structure of magnetotail reconnection revealed by mining space magnetometer data"

G. K. Stephens[1], M. I. Sitnov[1], R. S. Weigel[2], D. L. Turner[1], N. A. Tsyganenko[3], A. J. Rogers[4], K. Genestreti[5], and J. A. Slavin[6]

[1]The Johns Hopkins University Applied Physics Laboratory, Laurel, MD 20723, USA

[2]George Mason University, Fairfax, VA 22030, USA

[3]Saint-Petersburg State University, Saint-Petersburg, Russia

[4]University of New Hampshire, Durham, NH, USA

[5]Space Science and Engineering, Southwest Research Institute, Durham, NH, USA

[6]Department of Climate and Space Sciences and Engineering, University of Michigan, Ann Arbor, MI, USA

Contents of this file

Supporting Information Text

Space Magnetometer Data

The heritage of the space magnetometer data used in this study dates to earlier data mining (DM) reconstructions of storms (Sitnov et al., 2008). As this DM approach relies on knowledge of the solar wind plasma and IMF conditions, the start of the magnetometer archive (January 1995) was chosen to approximately coincide with the advent of continuous long-term L1 monitoring of the upstream solar wind which began in late 1994 with the launch of the Wind spacecraft. That archive (N. A. Tsyganenko & Sitnov, 2007) consisted of magnetic field observations from the IMP-8, Geotail, the Geosynchronous GOES-8, 9, 10, and 12 satellites, Cluster, and Polar missions. The time-resolution of the magnetometer data provided by the missions is often higher than is necessary for global scale reconstructions so it is common practice to downsample the original data source to a regular cadence by time-averaging over multiple measurements, e.g., (N. Tsyganenko et al., 2021). A decision must then be made for the frequency of the downsampled data. The archive from (N. A. Tsyganenko & Sitnov, 2007; Sitnov et al., 2008) choose 15 min averaging cadence except for when spacecraft were located within $r < 5R_E$, in which the higher spacecraft velocities prompted for a 5 min data cadence. This archive is available at http://geo.phys.spbu.ru/∼tsyganenko/data_sets.html.

The data archive from (N. A. Tsyganenko & Sitnov, 2007) was later augmented for the DM reconstructions of substorms by updating the Polar and Cluster datasets and by adding the THEMIS and Van Allen probes magnetometer data (Stephens et al., 2019). This expansion proved useful in populating the equatorial inner magnetosphere and near-tail region with data. In constructing this archive, the data from these four missions was averaged to a 5 min cadence, but when incorporated into the DM algorithm, it was downsampled to 15 min when the spacecraft location was $r \geq 5R_E$ to be consistent with the earlier archive. This database is available on the NASA Space Physics Data Facility: https://spdf.sci.gsfc.nasa.gov/pub/data/aaa_special-purpose-datasets/empirical-magnetic-field-modeling-database-with-TS07D-coefficients/. This was again extended in subsequent substorm reconstructions by adding the available MMS data, which at that time had completed a full season sampling the midtail following the extension of the MMS apogee to $r \approx 25R_E$ (Sitnov et al., 2019; Stephens & Sitnov, 2021). The addition of MMS data proved useful in the reconstruction of the mid-tail region including the resolution of X-line features (Sitnov et al., 2019). For these substorm reconstructions, data beyond the primary apogee of the Geotail mission, $r = 31R_E$, was filtered. This was performed primarily to remove data points from the two THEMIS probes as they transitioned to the ARTEMIS orbit, as the inclusion of this distant data could produce anomalous results (Stephens et al., 2019).

In this study, the magnetometer data archive has again been updated. Fist, given the importance of the MMS dataset to this particular investigation, it was extended through the end of the year 2020, now encompassing three full tail seasons. Further, in February of 2019, the MMS apogee was raised from $r \approx 25R_E$ to $r \approx 29R_E$ (Williams et al., 2020), increasing the amount of data in this region. Second, the THEMIS, Cluster, Van Allen Probes, and MMS datasets were all downsampled to a universal 5 min cadence, instead of switching between 5 and 15 min based on spacecraft's radial distance. The motivation being that the previous substorm investigations demonstrated that the DM approach can indeed reconstruct changes in the magnetosphere on the scale approaching 5 min resolution (Stephens et al., 2019; Sitnov et al., 2019). Further, this makes the cadence of the magnetometer archive consistent with that of the model reconstructions and the OMNI dataset. The remaining spacecraft datasets (Geotail, IMP-8, and GOES satellites) retain the 15 min data cadence only because upgrading them would require additional efforts beyond the scope of this study. The third is that the radial filter was increased from $31R_E$ to $36R_E$. Although, as Fig. S1 indicates, the data between $31R_E$ and $36R_E$ is relatively sparse, its inclusion was found to help stabilize the reconstructions in the region $r \approx 25$–$31R_E$, which was of particular importance for this study. The result is an archive of 8,649,672 magnetometer data records spanning the years 1995–2020 and radial distance 1.5 to $36R_E$. The resulting spatial distribution of the archive is shown in Fig. S1 while the breakdown of each individual spacecraft's contribution to the archive is displayed in Table S1.

The general process for constructing these datasets is as follows. First, the magnetometer data is downloaded from either the mission webpage or a community resource such as the NASA Space Physics Data Facility. Any anomalous data records are removed. The contribution of the internal magnetic field is removed utilizing the International Geomagnetic Reference Field (Alken et al., 2021) (IGRF model). Data collected when the spacecraft was outside the magnetopause is filtered by either visual determination of magnetopause crossings or by application of empirical magnetopause models, e.g., (Shue et al., 1998). The resulting data are then downsampled to the requisite data cadence using boxcar averaging. As one approaches the surface of the Earth, the value of the background magnetic field, B_{int}, becomes very large relative to the magnetic field generated by external current sources, B_{ext}. Thus, distinguishing the external and internal fields requires attitude knowledge beyond the capacity of many spacecraft missions. For these reasons data is excluded when $r < 1.5R_E$ for equatorial orbiting spacecraft. For polar orbiting spacecraft (Polar and Cluster), a larger exclusion radius of $r < 3.2R_E$ was used to prevent the large magnetic field deviations due to low-altitude FACs from biasing the fit.

Storm-Substorm-Solar Wind State-Space

Storms and substorms and their response to solar wind drivers have a tendency to develop in repeatable and predictable ways as indicated by their manifestation in geomagnetic indices, e.g., (Liemohn et al., 2018). This makes their empirical reconstruction using DM possible. To do this, the storm/substorm state of the magnetosphere is assumed to be characterizable using a low-dimensional state-space (Vassiliadis, 2006). For example, earlier storm studies formulated a 3D state-space based on the storm-time index *Sym-H*, its time derivative, and the solar wind electric field parameter vB_z^{IMF} (Sitnov et al., 2008) (where v is the X component of the solar wind bulk velocity which is multiplied by the Z component of the IMF in GSM coordinates), the idea being that these three parameters are representative of the storm state of the magnetosphere (Burton et al., 1975; Vassiliadis et al., 1999). At any given moment in time the storm-state of the magnetosphere is represented as a state-vector, $\mathbf{G}(t)$, within this state-space. As the storm develops, it will plot a trajectory through this state-space and similar events will trace similar trajectories. Subsequent substorm investigations expanded to a 5D state-space by adding the substorm index *AL* along with its time derivative (Stephens et al., 2019). For this study, the *AL* and *Sym-H* indices have been replaced by their SuperMAG counterparts (Gjerloev, 2012), *SML* and *SMR* respectively (Newell & Gjerloev, 2011, 2012). The primary reason for this change was that, as of the writing of this study, the digital values for the *AL* index are not available beyond March of 2018. This would have nullified the expansion of the MMS dataset discussed in the previous section. Further, although not officially authorized by the International Association of Geomagnetism and Aeronomy, the SuperMAG indices are computed using a much higher number of ground magnetometer stations (on the order of ~ 100 instead of ~ 10). In particular, the higher density and smaller gaps between stations allows the *SML* index to detect substorms that may be missed by the *AL* index (Newell & Gjerloev, 2011). As with the earlier studies, the storm index has been pressure corrected to remove magnetic perturbations caused by the compression of the magnetopause (Gonzalez et al., 1994). The pressure corrected index, *SMRc*, is defined: $SMRc = 0.8 \cdot SMR - 13\sqrt{P_{dyn}}$ (N. A. Tsyganenko et al., 2021). The 5D storm/substorm state-space used here is defined:

$$G_1^{(sst)}(t) = \langle SMRc| \propto \int_{-\Pi_{st}/2}^{0} SMRc(t+\tau)\cos(\pi\tau/\Pi_{st})\mathrm{d}\tau \tag{1}$$

$$G_2^{(sst)}(t) = \mathrm{D}\langle SMRc|/\mathrm{D}t \propto \int_{-\Pi_{st}/2}^{0} SMRc(t+\tau)\cos(2\pi\tau/\Pi_{st})\mathrm{d}\tau \tag{2}$$

$$G_3^{(sst)}(t) = \langle SML| \propto \int_{-\Pi_{sst}/2}^{0} SML(t+\tau)\cos(\pi\tau/\Pi_{sst})\mathrm{d}\tau \tag{3}$$

$$G_4^{(sst)}(t) = \mathrm{D}\langle SML|/\mathrm{D}t \propto \int_{-\Pi_{sst}/2}^{0} SML(t+\tau)\cos(2\pi\tau/\Pi_{sst})\mathrm{d}\tau \tag{4}$$

$$G_5^{(sst)}(t) = \langle vB_s^{IMF}| \propto \int_{0}^{\tau_\infty} vB_s^{IMF}(t-\tau_\infty+\tau)\exp\left[(\tau-\tau_\infty)/\tau_0\right]\mathrm{d}\tau \tag{5}$$

The integration convolves the original time-series data with smoothing windows. In the case of eq. (1) and eq. (3) the windows are half cosines which acts to smooth *SMRc* and *SML* over storm ($\Pi_{st}/2 = 6$ h) and substorms scales ($\Pi_{sst}/2 = 1$ h) respectively (Stephens et al., 2019). Meanwhile, their smoothed time derivatives, eq. (2) and eq. (4), are defined using two half cosine masks as described in (Sitnov et al., 2012). The fifth parameter, eq. (5), uses an exponential function to smooth over vB_s^{IMF} (where $B_s^{IMF} = -B_z^{IMF}$ when $B_z^{IMF} < 0$ and $B_s^{IMF} = 0$ otherwise). The exponential function not only acts as a smoothing window but also captures the loading of magnetic flux in the lobes during the substorm growth phase, thus, the e-folding time, $\tau_0 = 0.5$ h, was set based on the typical duration of the growth phase (Partamies et al., 2013). Six e-foldings were used in the convolution, $\tau_\infty = 6\tau_0$. Note, the integration only occurs over past data, as indicated by the limits of integration in eqs. (1)–(5), to prevent non-casual effects, that is, to prevent **G** from reacting to changes that have not yet occurred. The scale of each dimension of the state-space is standardized by dividing the above equations by their standard deviation (computed over the entirety of the state-space), as is indicated by the proportionality signs.

The solar wind plasma and IMF measurements were obtained from the NASA Space Physics Data Facility through OMNIWeb (https://omniweb.gsfc.nasa.gov/ow_min.html). OMNIWeb utilizes solar wind measurements from the ACE, Wind, IMP 8, and Geotail mission's magnetic field and plasma instruments applying a time delay to propagate them to the bow shock nose. The 5-min cadence OMNI products were used throughout this study, including the values for the solar wind velocity, flow pressure, and the IMF. The *SML* and *SMR* 1-min indices were downloaded through the SuperMAG webpage (https://supermag.jhuapl.edu/indices).

Mining Data Using k-Nearest Neighbors

Our approach resembles the k-Nearest Neighbor (kNN) method of data mining (DM) (Vassiliadis et al., 1995; Wettschereck et al., 1997), but also has important distinctions (Sitnov et al., 2008; Stephens et al., 2019). First, while the kNN subsets are first identified in the state-space, the magnetic field reconstruction is performed in the real space using magnetometer observations that occurred during those k_{NN} moments. The choice of the number of k_{NN} must be ample enough to fit flexible magnetic field models with high degrees of freedom (N. A. Tsyganenko & Sitnov, 2007; Stephens et al., 2019) while at the same time sufficiently small, $1 \ll k_{NN} \ll k_{SS}$ where k_{SS} is the number of points in the whole state-space, as to provide adequate sensitivity to the storm and substorm phases. Second, the state-space includes the smoothed time derivatives of the activity indices to increase the sensitivity of the DM procedure to these phases and to capture memory effects of the magnetosphere as a dynamic system (Sitnov et al., 2001).

In the DM method the state and input variables eqs. (1)–(5) are used to define the distance $R_q^{(i)} < R_{NN}$ of k_{NN} nearest neighbors from the query point $G_k^{(q)}$ $(k = 1, ..., 5)$:

$$R_q^{(i)} = \sqrt{\sum_{k=1}^{5} \left(G_k^{(i)} - G_k^{(q)}\right)^2 / \sigma_{G_k}^2}, \tag{6}$$

where each component is normalized by its standard deviation σ_{G_k}. Then the spatial reconstruction of the magnetic field for the event of interest is made using only a small $k_{NN} \ll k_{SS}$ part of the state-space with $k_{SS} \sim 4 \cdot 10^6$ points. Since the number of state-space points, k_{SS}, is quite large, the number of our instance-based subset k_{NN} can also be made sufficiently large to use for the magnetic field reconstruction a sufficiently flexible model with many degrees of freedom, which is described in the next section. The specific value of $k_{NN} = 32,000$ used in this study was found before (Stephens et al., 2019; Sitnov et al., 2019) to provide good validation results and resolve the spatial structure of the magnetic field and its evolution during substorms without overfitting.

Fitting the magnetic field data from the kNN subset is made by minimizing the distance in another, magnetic field vector space:

$$M_{err}^{(NN)} = \sqrt{\sum_{j \in S_{NN}} \sum_{i=x,y,z} w_j w_{(0)}(r) \left[B_i^{(mod)}(\mathbf{r}^{(j)}) - B_i^{j,obs}\right]^2}, \tag{7}$$

where $B_i^{j,obs}$ is the magnetic field record from the kNN subset S_{NN} (note that the number of observations in that subset is in general different from the number k_{NN}, because its depends on the number of probes available at any moment in time averaged over the subset;

the data structure of the database by mission is described in Table S1) and $B_i^{(mod)}(\mathbf{r}^{(j)})$ is the value of the jth magnetic field component of the model in the point of observation $\mathbf{r}^{(j)}$.

Note that the data points in the objective function eq. (7) are additionally weighted by the factor $w_{(0)}$ to mitigate the inhomogeneity of magnetometer records in the real space, which is seen from Fig. S1. In this weighting procedure, which is described in more detail in (N. A. Tsyganenko & Sitnov, 2007), the data is binned into $0.5R_E$ intervals of the geocentric distance r. Then the weight $w_{(0)}(r)$ is calculated as $\langle \Delta N \rangle / \max \{0.2\langle \Delta N \rangle, \Delta N_i\}$, where ΔN_i is the number of data points in the ith bin and $\langle \Delta N \rangle$ is the average number per bin over the entire set.

Another weighting w_j has been applied to mitigate the inhomogeneity of data in the state-space eqs. (1)–(5), with stronger data density for weaker solar wind/IMF input, storm and substorm activity (Stephens et al., 2020):

$$w_j = \exp\left[-\left(R_q^{(j)} / \sigma R_{NN} \right)^2 / 2 \right], \tag{8}$$

where R_{NN} is the radius of the NN sphere. The specific value of the weighting parameter $\sigma = 0.3$ used in this study was found in earlier studies to improve the spatial reconstruction and avoid overfitting for the chosen value of k_{NN} (Stephens et al., 2020).

Model Magnetic Field Architecture and Fitting Features

The analytical description of the magnetospheric magnetic field used in this study is nearly identical to that of earlier empirical reconstructions of substorms and is described in more detail in (Stephens et al., 2019). The total magnetospheric magnetic field, $\mathbf{B}_{tot}$ can be described as a summation of fields owing to individual current systems: $\mathbf{B}_{tot} = \mathbf{B}_{int} + \mathbf{B}_{FAC} + \mathbf{B}_{eq} + \mathbf{B}_{MP}$. The internal field, $\mathbf{B}_{int}$, is fundamentally different than the external fields as it is generated by currents deep in the Earth's interior, possesses a relatively slow rate of change (on the order of years), and is readily measured by ground based magnetometers. For these reasons, $\mathbf{B}_{int}$ is not considered within the scope of magnetospheric research and is represented by the IGRF model (Alken et al., 2021). Of interest are the magnetic fields generated by currents flowing within geospace, termed the external field, $\mathbf{B}_{ext}$. Specifically here, assuming the magnetopause as a perfectly conducting layer, the set of current systems is limited to those flowing within the magnetopause, the field-aligned currents $\mathbf{B}_{FAC}$ and equatorial currents $\mathbf{B}_{eq}$, and on the magnetopause $\mathbf{B}_{MP}$.

The building block for the equatorial current systems is the general solution of an infinitely thin arbitrarily distributed current sheet as detailed by (N. A. Tsyganenko & Sitnov, 2007). Solved in cylindrical coordinates (ρ,ϕ,z), the solution is composed of a Fourier series in ϕ and a Fourier-Bessel series in ρ, and the resulting magnetic field, $\mathbf{B}_{sheet}$, is given by a basis function expansion having the form:

$$\mathbf{B}_{sheet}(\rho, \phi, z) = \sum_{n=1}^{N} a_{0n}^{(s)} \mathbf{B}_{0n}^{(s)} + \sum_{m=1}^{M} \sum_{n=1}^{N} (a_{mn}^{(o)} \mathbf{B}_{mn}^{(o)} + a_{mn}^{(e)} \mathbf{B}_{mn}^{(e)}). \tag{9}$$

where $\mathbf{B}_{0n}$, $\mathbf{B}_{mn}^{(o)}$, and $\mathbf{B}_{mn}^{(e)}$ are basis functions with axially symmetry, odd (sine), and even (cosine) symmetry respectively; while a_{mn} are the amplitude coefficients.

Note, although this yields an arbitrary description in ρ and ϕ, its structure in z is rigidly defined to be an infinitely thin current sheet at $z = 0$. However, the Dirac delta profile of the current density in z can be broadened into a realistic finite distribution by performing the variable substitution $\zeta = \sqrt{z^2 + D^2}$, introducing the parameter D as the current sheet half-thickness. The thickness parameter D need not be a constant but can take the form of any differentiable function $D = D(\rho, \phi)$.

A distinctive feature of the tail is the formation of multiscale current sheets in the substorm growth phase with an ion-scale thin current sheet (TCS) embedded into a much thicker current sheet (Sergeev et al., 2011). In order to capture this feature, (Stephens et al., 2019) used two such expansions to describe the equatorial field:

$$\mathbf{B}^{(eq)}(\rho, \phi, z) = \mathbf{B}^{(eq)}(\rho, \phi, z; D) + \mathbf{B}^{(eq)}(\rho, \phi, z; D_{TCS}), \tag{10}$$

where D_{TCS} is constrained to be $D_{TCS} < D$. Further studies (Stephens et al., 2019; Sitnov et al., 2019) confirmed the buildup of TCS in the growth phase of substorms and their decay during the expansion and recovery phases.

Earlier studies assumed a spatially constant TCS thickness, $D_{TCS} = const$, although it was allowed to vary in time (Stephens et al., 2019). Here, the embedded TCS structure has been further generalized to verify the possible physical mechanisms of the TCS formation. It can be explained, e.g., (Sitnov et al., 2006), by figure-eight like (Speiser) proton orbits (Speiser, 1965). If this is the case, the parameter D_{TCS} of the magnetic field model should depend on the distance ρ from the Earth because the Speiser orbit size, ρ_{Si}, is inversely proportional to the magnetic field outside the sheet, B_L, which itself depends on ρ (Wang et al., 2004). To take this effect into account, the magnetic field architecture was further generalized using the approximation eq. (11) with free parameters α, β and D_0 and x_0 to be inferred from data.

$$D_{TCS}(x,y) = \left(\alpha e^{-\beta\rho'} + D_0^{-1}\right)^{-1}, \rho' = \sqrt{(x-x_0)^2 + y^2}. \qquad (11)$$

The results of the fitting the TCS thickness model eq. (11) with data within the framework of the DM-based global magnetic field reconstruction using a generalization of the basis-function expansion eq. (9) for variable TCS thickness (eqs.(15)-(17) in (N. A. Tsyganenko & Sitnov, 2007)) are presented in Fig. S2 for the main group of IDR events, G, M, W, and Y. Similar profiles of the lobe field B_L and the inverse TCS thickness D_{TCS} seen in this figure suggest that the TCS thickness scales as the thermal ion gyroradius in the field B_L and hence its is likely formed by quasi-adiabatic (Speiser) ions (Speiser, 1965; Sitnov et al., 2006). The value of D_{TCS} asymptotically approaches D_0 at increasing distance, with the constraint $D_0 \leq D$, so that D_{TCS} cannot exceeds the thickness of the thick sheet.

A further complication is that the equatorial current system rarely lies in a plane centered about $z = 0$. The Earth's dipole axis is not generally orthogonal to the direction of the solar wind flow. The angle that the dipole axis makes with the Z axis of the Geocentric Solar Magnetic (GSM) coordinate system is the "dipole tilt angle". Its finite value may cause bending and warping of the tail current sheet while changes in the IMF clock angle (the angle between geomagnetic north and the projection of the IMF vector onto the GSM Y-Z plane) may twist the current sheet (N. A. Tsyganenko & Fairfield, 2004). These effects can be accounted for by application of the general deformation technique (N. A. Tsyganenko, 1998). Specifically, here the "bowl-shaped" deformation from (N. A. Tsyganenko, 2014) is used, introducing three additional free parameters which define the center of the current sheet; the hinging distance R_H, the warping parameter G, and the twisting parameter TW.

The values of M and N determine the number of azimuthal and radial expansions in equation (9) and thus the resolution of the equatorial currents in ϕ and ρ respectively. Here, as with previous substorm investigations (Stephens et al., 2019), $(M, N) = (6, 8)$ as this was determined a sufficient resolution to resolve current structure throughout the near and mid-tail without overfitting to data (Stephens & Sitnov, 2021). Further, as with the prior investigations, in order to account for potential dynamical pressure effects on the structure of equatorial currents, each of the amplitude coefficient terms in eq. (9) are made explicit functions of P_{dyn}: $a^{(\gamma)}_{\alpha\beta} \rightarrow a^{(\gamma)}_{0,\alpha\beta} + a^{(\gamma)}_{1,\alpha\beta}\sqrt{P_{dyn}}$, doubling their number. The end result is a total of 416 amplitude coefficients which determine the spatial structure of the equatorial current sheet.

The FAC magnetic field, $\mathbf{B}_{FAC}$, module used in this study is identical to that of (Stephens et al., 2019). The foundation of their analytical description are the radially flowing conical current systems developed in (N. Tsyganenko, 1991), which are then bent to follow approximately dipolar field lines using the general deformation technique which also accounts for the day-night asymmetry (N. A. Tsyganenko, 2002a). The azimuthal dependence of the conical currents utilizes a Fourier series, giving them flexibility to reconstruct the magnetic local time variations of the FACs but at the expense of having a very rigid latitudinal structure. In order to mimic expansion like flexibility in latitude, four such conical current systems are placed at overlapping latitudes. The first four Fourier terms are used for each of the four latitudinal varying conical currents resulting in a total of 16 linear amplitude coefficients that determine the FACs spatial structure. Global rescaling parameters were introduced to allow the FACs to shrink and grow in response to storm and substorm phases. Instead of allowing each of the four current systems to rescale independently, the two higher latitude systems were tied to one parameter κ_{R1} and the two lower to another κ_{R2}. The values of κ_{R1} and κ_{R2} were constrained so that they approximated the region-1 and region-2 current systems respectively. This formulation was shown to successfully reproduce the more complex spiral like FAC pattern observed in the AMPERE data (Sitnov et al., 2017).

Unlike the other external fields, in which the magnetic field sought is consistent with some conceptualization of a current system, the magnetopause magnetic field, $\mathbf{B}_{MP}$, does not attempt to represent a current. Instead, the domain of validity of the model is restricted to just inside the magnetopause current layer, where $\mathbf{j}_{MP} = 0$. Thus, $\mathbf{B}_{MP}$ is irrotational and can be represented by a magnetic scalar potential, $\mathbf{B}_{MP} = -\nabla U$ and its formulation is simply the solution to Laplace's equation: $\nabla^2 U = 0$ (N. A. Tsyganenko, 2014). In this context, $\mathbf{B}_{MP}$ is termed a shielding field in that it ensures the magnetosphere is closed, that is, that field lines do not cross the magnetopause. A closed magnetosphere is represented by the condition $\mathbf{B}_{tot} \cdot \mathbf{n}|_S = 0$, where S is the modeled magnetopause boundary and $\mathbf{n}$ is the normal to that surface. Here, as with previous studies, S is defined as the Shue magnetopause (Shue et al., 1998). In practice it is more tractable to represent $\mathbf{B}_{MP}$ as a combination of shielding fields: $\mathbf{B}_{MP} = \mathbf{B}_{int}^{(sh)} + \mathbf{B}_{FAC}^{(sh)} + \mathbf{B}_{eq}^{(sh)}$; that way, each shielding field can be formulated independently using a coordinate system and geometry that makes sense for that particular system. For example, owing to the cylindrical geometry of $\mathbf{B_{eq}}$, U_{eq} is represented by an expansion of Fourier-Bessel harmonics, eq. 20 of (N. A. Tsyganenko & Sitnov, 2007), while U_{int} and U_{FAC} utilize an expansion of "Box" harmonics, appendix of (N. A. Tsyganenko, 1998) and eq. 34 of (N. A. Tsyganenko, 1995) respectively. S is then sampled to a distance of $r \sim 50R_E$ and the shielding field expansion (e.g., $\mathbf{B}_{eq}^{(sh)} = -\nabla U_{eq}$) and the shielded field (e.g., $\mathbf{B_{eq}}$) are evaluated at the location of each sample. This allows the coefficients of the shielding field expansion (e.g. U_{eq}) to be found by minimizing the normal component of the combined field at the magnetopause boundary, e.g., min $\left[(\mathbf{B}_{eq,j} + \mathbf{B}_{eq,j}^{(sh)}) \cdot \mathbf{n}_j\right]$. For a more thorough discussion on this topic see (N. A. Tsyganenko, 2014).

One more consideration built into the structure of the model is the magnetosphere's expansion and contraction in response to changes in the solar wind dynamical pressure, P_{dyn}. It is well established from observations of magnetopause crossings that the magnetopause responds to decreases/increases in the solar wind dynamical pressure, P_{dyn}, by expanding/contracting in a self-similar way, that is, its size changes but not its shape, e.g., (Sibeck et al., 1991; Shue et al., 1998). This self-similarity is easily represented by rescaling the position vector as a function of P_{dyn}. Using simple pressure balance considerations the functional form of this rescaling is $\mathbf{r'} = {P_{dyn}}^{-\kappa}$, where $\kappa = 1/6$ for a perfect dipole (Mead & Beard, 1964). Here, as with many previous empirical studies, all current systems are assumed to possess the same self-similarity rescaling, that is they all take the same functional form and same value of κ (N. A. Tsyganenko, 2014). This assumption simplifies the shielding of these fields as both the shielded and the shielding fields rescale together. κ could be treated as a free parameter when the model is fit to data, however, previous studies have shown κ to be relatively stable (N. A. Tsyganenko, 2002b), so here a constant value of $\kappa = 0.155$ from (N. A. Tsyganenko & Sitnov, 2007) was used.

The final magnetic field model configuration includes 432 linear amplitude coefficients and 10 free non-linear parameters D,α,β,D_0,x_0,R_H,G,TW,κ_{R1},κ_{R2} which are determined by fitting them to the identified subset of magnetometer data. The linear coefficients are determined by applying the singular value decomposition pseudo-inversion method to the overdetermined linear least squares problem (Jackson, 1972; Press et al., 1992). The non-linear parameters are found by embedding the linear solver within the Nelder-Mead downhill simplex algorithm (Nelder & Mead, 1965).

Ion Diffusion Region Alphabet

The whole set of 26 IDR events detected by MMS in 2017–2020 (A. J. Rogers et al., 2019; A. Rogers et al., 2021) (labeled in our study by letters A-Z) are listed in Table S2. The second column in the table lists the starting date and time of each IDR interval suggested by MMS (A. J. Rogers et al., 2019; A. Rogers et al., 2021), while the third column indicates the corresponding model time resulting from the adopted 5-min cadence. The forth and fifth columns show the distances between the MMS tetrahedron and reconstructed contours $B_z = 0$ nT and $B_z = 2$ nT. The distance is found as the minimum radius of the 3D sphere, which crosses the corresponding $B_z = const$ contour.

Based on this, we can categorize our 16 “Hits” as $D_{0nT} < 2.0R_E$, which includes 11 X-lines (A, C, D, E, G, Q, S, V, W, X, Y) and 5 O-lines (H, L, M, O, R). “Near hits” would then be events that miss the 0 nT contour, but instead hit the 2 nT, $D_{2nT} < 2.2R_E$ (< 2 nT for all events except N). This would give us 8 more "Near hits" (I, J, K, N, P, T, U, Z). Our 2 "Misses" (B, F) are then events where both $D_{0nT} \geq 2.0R_E$ and $D_{2nT} \geq 2.2R_E$. These quantitative estimates support the qualitative characterization of the DM fidelity in the $B_z = 0$ contour reconstruction provided in the main text of the paper. The sixth column indicates the figures where the corresponding IDRs are plotted against the corresponding equatorial B_z and meridional current distributions.

Additional IDR Hits

Figs. S3–S8 and S9–S14 show the results of the comparison of the equatorial and meridional magnetic field distributions with the locations of MMS IDRs (A. J. Rogers et al., 2019; A. Rogers et al., 2021) in the formats similar to Figs. 2 and 3 for the rest of the IDR alphabet.

Special considerations were taken in regards to events R and T. In the first case, the initial reconstruction placed the location of the central plasma sheet $\sim 3R_E$ below the MMS spacecraft during the IDR observation. Upon further inspection, the event was found to have an anomalously large value of B_y^{IMF} over the preceding 30-min, with a value of $8nT$. Large magnitudes of y component of the IMF are known to significantly impact the shape of the magnetotail specifically through the twisting of the plasma sheet (N. A. Tsyganenko & Fairfield, 2004). Although this feature is included in the structure of the model through the warping and twisting deformation equations, specifically via the parameter TW in (N. A. Tsyganenko, 1998), its impact is presumably not captured in the storm/substorm state-space represented by eqs. (1)–(5). Indeed, computing TW using the empirical relationship from (N. A. Tsyganenko & Fairfield, 2004) (see their eq. 1 and eq. 5), results in $TW = 1.11 \times 10^{-2}$, the largest magnitude across all 26 events and being a factor of two larger than the next highest and a factor of five higher than the average event. Thus, event R was reconstructed using this empirical value and not the value obtained during the fit ($TW = 2.64 \times 10^{-3}$). As earlier studies using the SST19 model were primarily concerned with the inner magnetosphere and/or the near-tail region, they probably neglected to observe this inconsistency. In future studies, particularly of the mid-tail, this issue should be remedied. One potential solution is to explicitly add a dimension to the state-space that correlates to the twisting effect, for instance the value of B_y^{IMF} itself or the IMF clock angle. However, owing to the "curse of dimensionality" (Verleysen & François, 2005), expanding the state-space may dilute its sensitivity to the storm and substorm features sought. Another solution that is potentially more robust is to exclude TW from the set of free parameters that is determined when fitting to data and instead replace it with an ad-hoc functional form such as the empirical relationship from (N. A. Tsyganenko & Fairfield, 2004).

In event T, the original reconstruction with $\sigma = 0.3$ underresolved the X-line, apparently because of the unusual IMF structure ($|B_z| \sim |B_x| \sim |B_y| \sim 6$ nT). To mitigate this issue, we slightly reduced the weighting parameter to $\sigma = 0.25$.

References

Alken, P., Thébault, E., Beggan, C. D., Amit, H., Aubert, J., Baerenzung, J., . . . Zhou, B. (2021, December). International geomagnetic reference field: the thirteenth generation. *Earth, Planets and Space*, *73*(1), 49. doi: 10.1186/s40623-020-01288-x

Burton, R. K., McPherron, R. L., & Russell, C. T. (1975). An empirical relationship between interplanetary conditions and dst. *Journal of Geophysical Research (1896-1977)*, *80*(31), 4204-4214. doi: https://doi.org/10.1029/JA080i031p04204

Gjerloev, J. W. (2012). The supermag data processing technique. *Journal of Geophysical Research: Space Physics*, *117*(A9), https://doi.org/10.1029/2012JA017683. doi: https://doi.org/10.1029/2012JA017683

Gonzalez, W. D., Joselyn, J. A., Kamide, Y., Kroehl, H. W., Rostoker, G., Tsurutani, B. T., & Vasyliunas, V. M. (1994). What is a geomagnetic storm? *Journal of Geophysical Research: Space Physics*, *99*(A4), 5771-5792. Retrieved from `https://agupubs.onlinelibrary.wiley.com/doi/abs/10.1029/93JA02867` doi: https://doi.org/10.1029/93JA02867

Jackson, D. D. (1972, 06). Interpretation of Inaccurate, Insufficient and Inconsistent Data. *Geophysical Journal International*, *28*(2), 97-109. Retrieved from `https://doi.org/10.1111/j.1365-246X.1972.tb06115.x` doi: 10.1111/j.1365-246X.1972.tb06115.x

Li, T., Priest, E., & Guo, R. (2021). Three-dimensional magnetic reconnection in astrophysical plasmas. *Proc. Royal Soc. A*, *477*(2249), 10.1098/rspa.2020.0949. doi: 10.1098/rspa.2020.0949

Liemohn, M. W., McCollough, J. P., Jordanova, V. K., Ngwira, C. M., Morley, S. K., Cid, C., . . . Vasile, R. (2018). Model evaluation guidelines for geomagnetic index predictions. *Space Weather*, *16*(12), 2079-2102. Retrieved from `https://agupubs.onlinelibrary.wiley.com/doi/abs/10.1029/2018SW002067` doi: https://doi

.org/10.1029/2018SW002067

Mead, G. D., & Beard, D. B. (1964). Shape of the geomagnetic field solar wind boundary. *Journal of Geophysical Research (1896-1977)*, *69*(7), 1169-1179. Retrieved from https://agupubs.onlinelibrary.wiley.com/doi/abs/10.1029/JZ069i007p01169 doi: https://doi.org/10.1029/JZ069i007p01169

Nelder, J. A., & Mead, R. (1965, 01). A Simplex Method for Function Minimization. *The Computer Journal*, *7*(4), 308-313. Retrieved from https://doi.org/10.1093/comjnl/7.4.308 doi: 10.1093/comjnl/7.4.308

Newell, P. T., & Gjerloev, J. W. (2011). Evaluation of supermag auroral electrojet indices as indicators of substorms and auroral power. *Journal of Geophysical Research: Space Physics*, *116*(A12), https://doi.org/10.1029/2011JA016779. Retrieved from https://agupubs.onlinelibrary.wiley.com/doi/abs/10.1029/2011JA016779 doi: https://doi.org/10.1029/2011JA016779

Newell, P. T., & Gjerloev, J. W. (2012). Supermag-based partial ring current indices. *Journal of Geophysical Research: Space Physics*, *117*(A5), https://doi.org/10.1029/2012JA017586. Retrieved from https://agupubs.onlinelibrary.wiley.com/doi/abs/10.1029/2012JA017586 doi: https://doi.org/10.1029/2012JA017586

Partamies, N., Juusola, L., Tanskanen, E., & Kauristie, K. (2013). Statistical properties of substorms during different storm and solar cycle phases. *Annales Geophysicae*, *31*(2), 349–358. Retrieved from https://www.ann-geophys.net/31/349/2013/ doi: 10.5194/angeo-31-349-2013

Press, W. H., Teukolsky, S. A., Flannery, B. P., & Vetterling, W. T. (1992). *Numerical recipes in fortran: The art of scientific computing* (2nd ed.). USA: Cambridge University Press.

Rogers, A., Farrugia, C. J., Torbert, R. B., & Rogers, T. J. (2021). Applying magnetic curvature to to MMS data to identify thin current sheets relative to tail reconnection. *Earth and Space Science Open Archive*, 12. doi: 10.1002/essoar.10509282.1

Rogers, A. J., Farrugia, C. J., & Torbert, R. B. (2019). Numerical algorithm for detecting ion diffusion regions in the geomagnetic tail with applications to mms tail season 1 may to 30 september 2017. *Journal of Geophysical Research: Space Physics*, *124*(8), 6487-6503. Retrieved from `https://agupubs.onlinelibrary.wiley.com/doi/abs/10.1029/2018JA026429` doi: https://doi.org/10.1029/2018JA026429

Sergeev, V., Angelopoulos, V., Kubyshkina, M., Donovan, E., Zhou, X.-Z., Runov, A., ... Nakamura, R. (2011). Substorm growth and expansion onset as observed with ideal ground-spacecraft themis coverage. *Journal of Geophysical Research: Space Physics*, *116*(A5), https://doi.org/10.1029/2010JA015689. doi: https://doi.org/10.1029/2010JA015689

Shue, J.-H., Song, P., Russell, C. T., Steinberg, J. T., Chao, J. K., Zastenker, G., ... Kawano, H. (1998). Magnetopause location under extreme solar wind conditions. *Journal of Geophysical Research: Space Physics*, *103*(A8), 17691-17700. doi: https://doi.org/10.1029/98JA01103

Sibeck, D. G., Lopez, R. E., & Roelof, E. C. (1991). Solar wind control of the magnetopause shape, location, and motion. *Journal of Geophysical Re-*

search: Space Physics, *96*(A4), 5489-5495. Retrieved from https://agupubs.onlinelibrary.wiley.com/doi/abs/10.1029/90JA02464 doi: https://doi.org/10.1029/90JA02464

Sitnov, M. I., Sharma, A. S., Papadopoulos, K., & Vassiliadis, D. (2001, Dec). Modeling substorm dynamics of the magnetosphere: From self-organization and self-organized criticality to nonequilibrium phase transitions. *Phys. Rev. E*, *65*, 016116. Retrieved from https://link.aps.org/doi/10.1103/PhysRevE.65.016116 doi: 10.1103/PhysRevE.65.016116

Sitnov, M. I., Stephens, G. K., Tsyganenko, N. A., Miyashita, Y., Merkin, V. G., Motoba, T., … Genestreti, K. J. (2019). Signatures of nonideal plasma evolution during substorms obtained by mining multimission magnetometer data. *Journal of Geophysical Research: Space Physics*, *124*(11), 8427-8456. doi: 10.1029/2019JA027037

Sitnov, M. I., Stephens, G. K., Tsyganenko, N. A., Ukhorskiy, A. Y., Wing, S., Korth, H., & Anderson, B. J. (2017). Spatial structure and asymmetries of magnetospheric currents inferred from high-resolution empirical geomagnetic field models. In *Dawn-dusk asymmetries in planetary plasma environments* (p. 199-212). American Geophysical Union (AGU). doi: 10.1002/9781119216346.ch15

Sitnov, M. I., Swisdak, M., Guzdar, P. N., & Runov, A. (2006). Structure and dynamics of a new class of thin current sheets. *Journal of Geophysical Research: Space Physics*, *111*(A8), https://doi.org/10.1029/2005JA011517. doi: https://doi.org/10.1029/2005JA011517

Sitnov, M. I., Tsyganenko, N. A., Ukhorskiy, A. Y., & Brandt, P. C. (2008). Dynamical data-based modeling of the storm-time geomagnetic field with enhanced spatial resolution. *Journal of Geophysical Research: Space Physics*, *113*(A7), 10.1029/2007JA013003. doi: 10.1029/2007JA013003

Sitnov, M. I., Ukhorskiy, A. Y., & Stephens, G. K. (2012). Forecasting of global data-binning parameters for high-resolution empirical geomagnetic field models. *Space Weather*, *10*(9), 10.1029/2012SW000783. doi: 10.1029/2012SW000783

Speiser, T. W. (1965). Particle trajectories in model current sheets: 1. analytical solutions. *Journal of Geophysical Research (1896-1977)*, *70*(17), 4219-4226. doi: https://doi.org/10.1029/JZ070i017p04219

Stephens, G. K., Bingham, S. T., Sitnov, M. I., Gkioulidou, M., Merkin, V. G., Korth, H., … Ukhorskiy, A. Y. (2020). Storm time plasma pressure inferred from multimission measurements and its validation using van allen probes particle data. *Space Weather*, *18*(12), e2020SW002583. doi: https://doi.org/10.1029/2020SW002583

Stephens, G. K., & Sitnov, M. I. (2021). Concurrent empirical magnetic reconstruction of storm and substorm spatial scales using data mining and virtual spacecraft. *Frontiers in Physics*, *9*, 210. Retrieved from `https://www.frontiersin.org/article/10.3389/fphy.2021.653111` doi: 10.3389/fphy.2021.653111

Stephens, G. K., Sitnov, M. I., Korth, H., Tsyganenko, N. A., Ohtani, S., Gkioulidou, M., & Ukhorskiy, A. Y. (2019). Global empirical picture of magnetospheric substorms inferred from multimission magnetometer data. *Journal of Geophysical Research: Space Physics*, *124*(2), 1085-1110. Retrieved from `https://agupubs.onlinelibrary.wiley.com/doi/abs/10.1029/2018JA025843` doi: 10.1029/2018JA025843

Tsyganenko, N. (1991). Methods for quantitative modeling of the magnetic field from Birkeland currents. *Planetary and Space Science*, *39*(4), 641 - 654. Retrieved from http://www.sciencedirect.com/science/article/pii/003206339190058I doi: http://dx.doi.org/10.1016/0032-0633(91)90058-I

Tsyganenko, N., Andreeva, V., Kubyshkina, M., Sitnov, M., & Stephens, G. (2021). Data-based modeling of the earth's magnetic field. In *Magnetospheres in the solar system* (p. 617-635). American Geophysical Union (AGU). Retrieved from https://agupubs.onlinelibrary.wiley.com/doi/abs/10.1002/9781119815624.ch39 doi: https://doi.org/10.1002/9781119815624.ch39

Tsyganenko, N. A. (1995). Modeling the earth's magnetospheric magnetic field confined within a realistic magnetopause. *Journal of Geophysical Research: Space Physics*, *100*(A4), 5599-5612. doi: https://doi.org/10.1029/94JA03193

Tsyganenko, N. A. (1998). Modeling of twisted/warped magnetospheric configurations using the general deformation method. *Journal of Geophysical Research: Space Physics*, *103*(A10), 23551-23563. Retrieved from https://agupubs.onlinelibrary.wiley.com/doi/abs/10.1029/98JA02292 doi: https://doi.org/10.1029/98JA02292

Tsyganenko, N. A. (2002a). A model of the near magnetosphere with a dawn-dusk asymmetry 1. Mathematical structure. *Journal of Geophysical Research: Space Physics*, *107*(A8), SMP 12-1-SMP 12-15. doi: 10.1029/2001JA000219

Tsyganenko, N. A. (2002b). A model of the near magnetosphere with a dawn-dusk asymmetry 2. parameterization and fitting to observations. *Jour-*

nal of Geophysical Research: Space Physics, *107*(A8), SMP 10-1-SMP 10-17. Retrieved from https://agupubs.onlinelibrary.wiley.com/doi/abs/10.1029/2001JA000220 doi: https://doi.org/10.1029/2001JA000220

Tsyganenko, N. A. (2014). Data-based modeling of the geomagnetosphere with an imf-dependent magnetopause. *Journal of Geophysical Research: Space Physics*, *119*(1), 335-354. doi: 10.1002/2013JA019346

Tsyganenko, N. A., Andreeva, V. A., Sitnov, M. I., Stephens, G. K., Gjerloev, J. W., Chu, X., & Troshichev, O. A. (2021). Reconstructing substorms via historical data mining: Is it really feasible? *Journal of Geophysical Research: Space Physics*, *126*(10), e2021JA029604. doi: https://doi.org/10.1029/2021JA029604

Tsyganenko, N. A., & Fairfield, D. H. (2004). Global shape of the magnetotail current sheet as derived from geotail and polar data. *Journal of Geophysical Research: Space Physics*, *109*(A3), https://doi.org/10.1029/2003JA010062. doi: https://doi.org/10.1029/2003JA010062

Tsyganenko, N. A., & Sitnov, M. I. (2007). Magnetospheric configurations from a high-resolution data-based magnetic field model. *Journal of Geophysical Research: Space Physics*, *112*(A6), 10.1029/2007JA012260. doi: 10.1029/2007JA012260

Vassiliadis, D. (2006). Systems theory for geospace plasma dynamics. *Reviews of Geophysics*, *44*(2), https://doi.org/10.1029/2004RG000161. doi: https://doi.org/10.1029/2004RG000161

Vassiliadis, D., Klimas, A., & Baker, D. (1999). Models of dst geomagnetic activity and of its coupling to solar wind parameters. *Physics and Chemistry of the Earth, Part C:*

Solar, Terrestrial & Planetary Science, *24*(1), 107-112. Retrieved from https://www.sciencedirect.com/science/article/pii/S1464191798000166 (International Symposium on Solar-Terrestrial Coupling Processes) doi: https://doi.org/10.1016/S1464-1917(98)00016-6

Vassiliadis, D., Klimas, A. J., Baker, D. N., & Roberts, D. A. (1995). A description of the solar wind-magnetosphere coupling based on nonlinear filters. *Journal of Geophysical Research: Space Physics*, *100*(A3), 3495-3512. Retrieved from https://agupubs.onlinelibrary.wiley.com/doi/abs/10.1029/94JA02725 doi: https://doi.org/10.1029/94JA02725

Verleysen, M., & François, D. (2005). The curse of dimensionality in data mining and time series prediction. In J. Cabestany, A. Prieto, & F. Sandoval (Eds.), *Computational intelligence and bioinspired systems* (pp. 758–770). Berlin, Heidelberg: Springer Berlin Heidelberg.

Wang, C.-P., Lyons, L. R., Nagai, T., & Samson, J. C. (2004). Midnight radial profiles of the quiet and growth-phase plasma sheet: The geotail observations. *Journal of Geophysical Research: Space Physics*, *109*(A12), https://doi.org/10.1029/2004JA010590. doi: https://doi.org/10.1029/2004JA010590

Wettschereck, D., Aha, D. W., & Mohri, T. (1997, Feb 01). A review and empirical evaluation of feature weighting methods for a class of lazy learning algorithms. *Artificial Intelligence Review*, *11*(1), 273-314. Retrieved from https://doi.org/10.1023/A:1006593614256 doi: 10.1023/A:1006593614256

Williams, T., Shulman, S., Ottenstein, N., Palmer, E., Riley, C., Letourneau, S., … Godine, D. (2020). Operational techniques for dealing with long eclipses during the mms extended mission. In *2020 ieee aerospace conference* (p. 1-12). doi: 10.1109/AERO47225.2020.9172276

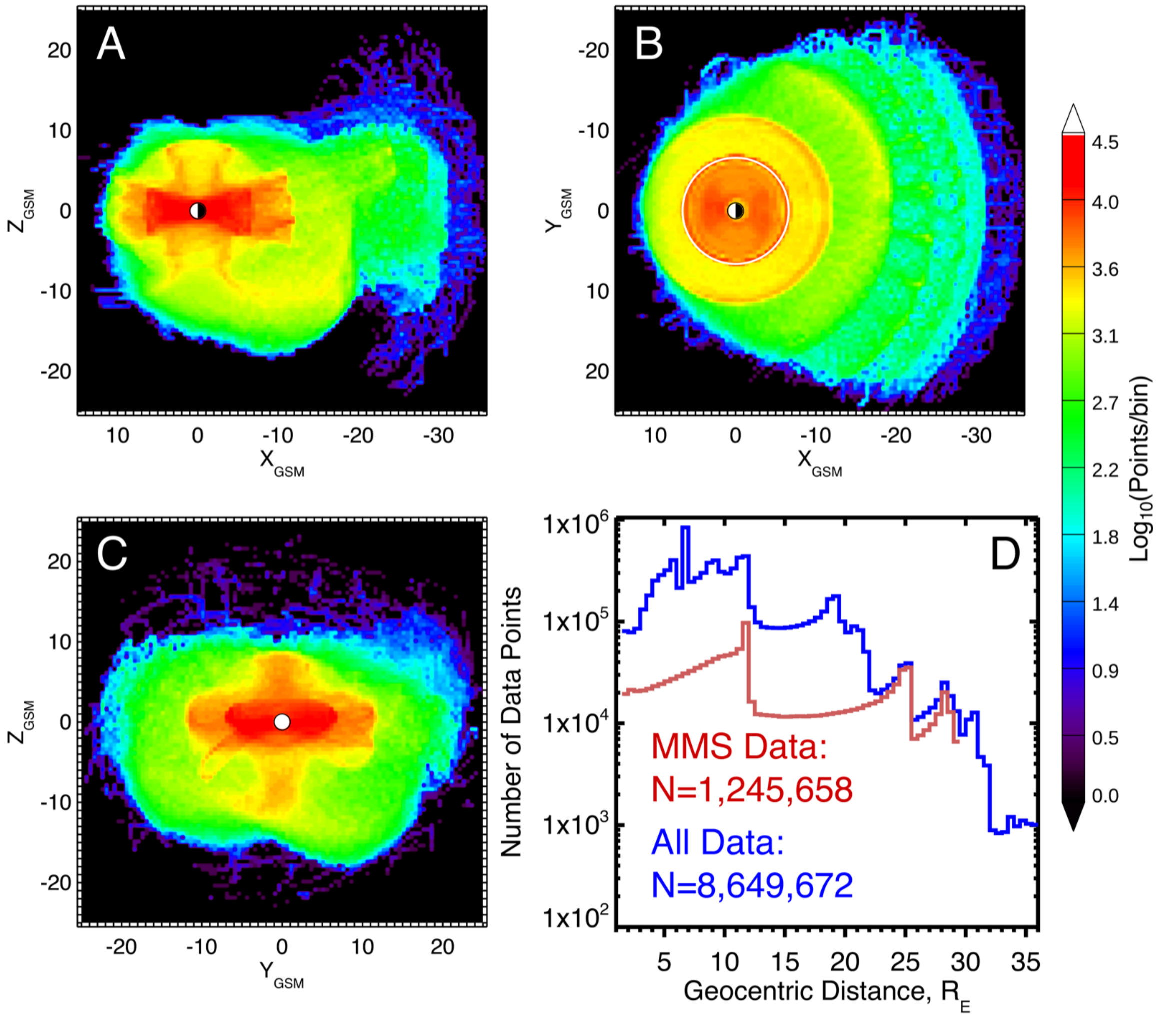

Figure S1. Distribution of data points in the archive of space magnetometer Data. (A, B, and D) A 2D histogram displaying the spatial distribution a data points projected into the meridional (A), equatorial (B), and Y-Z (C) planes in the GSM coordinate system. The color indicates the number of points in each $0.5R_E$ by $0.5R_E$ bin using a logarithmic scale, with red/purple corresponding to regions with a dense/sparse density of data points. Black regions contain zero data points. (D) A 1D histogram showing the number of data points in $0.5R_E$ radial bins (spherical shells) using a logarithmic scale with the total archive in blue and just the MMS dataset in red.

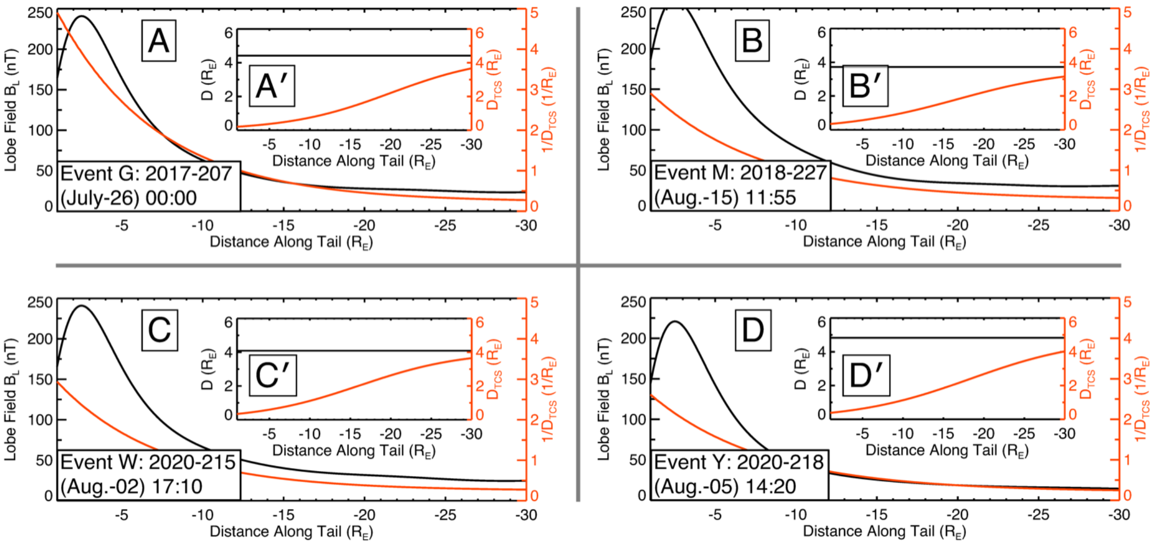

Figure S2. Profiles of the lobe field B_L and current sheet thicknesses along the tail. (A-D) 1D profiles of the for B_L (black line) and the inverse TCS thickness $1/D_{TCS}$ (orange line) sampled at midnight ($y = 0$) along the tail for four IDR events, G, M, W, and Y. B_L is evaluated at a height of $z = 5R_E$ above the center of the current sheet. The inset panels (A'-D') show the value 1D profiles of the current sheet thickness for the thick sheet (black constant line) and D_{TCS} (orange line).

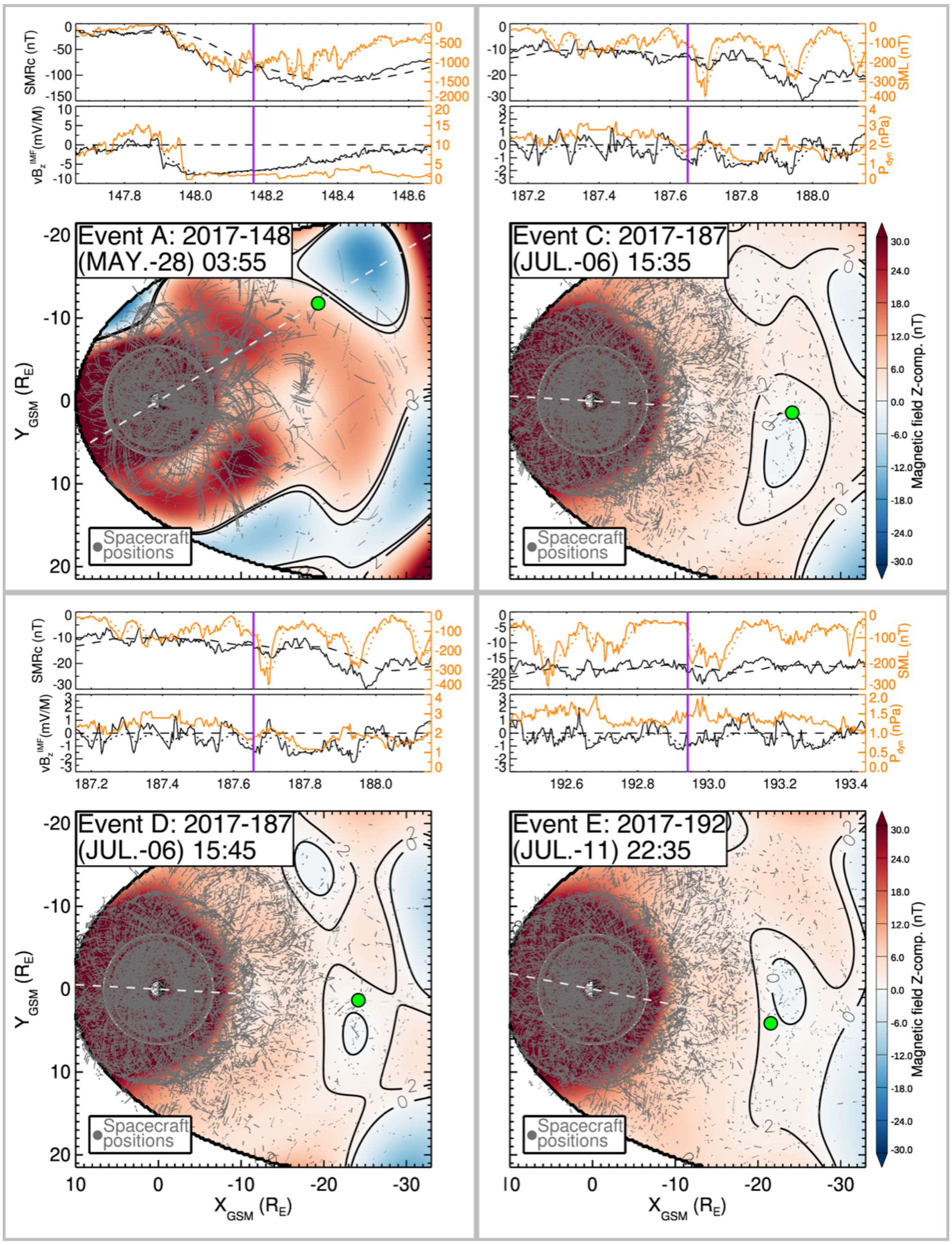

Figure S3. Ion diffusion regions and the equatorial magnetic field landscape. The format is similar to Fig. 2 except for a different group of IDR events: A, C, D, and E, which are marked here by purple dots. These four events are considered "hits" as the $B_z = 0$ contour is within $< 2R_E$ of the observed MMS IDR.

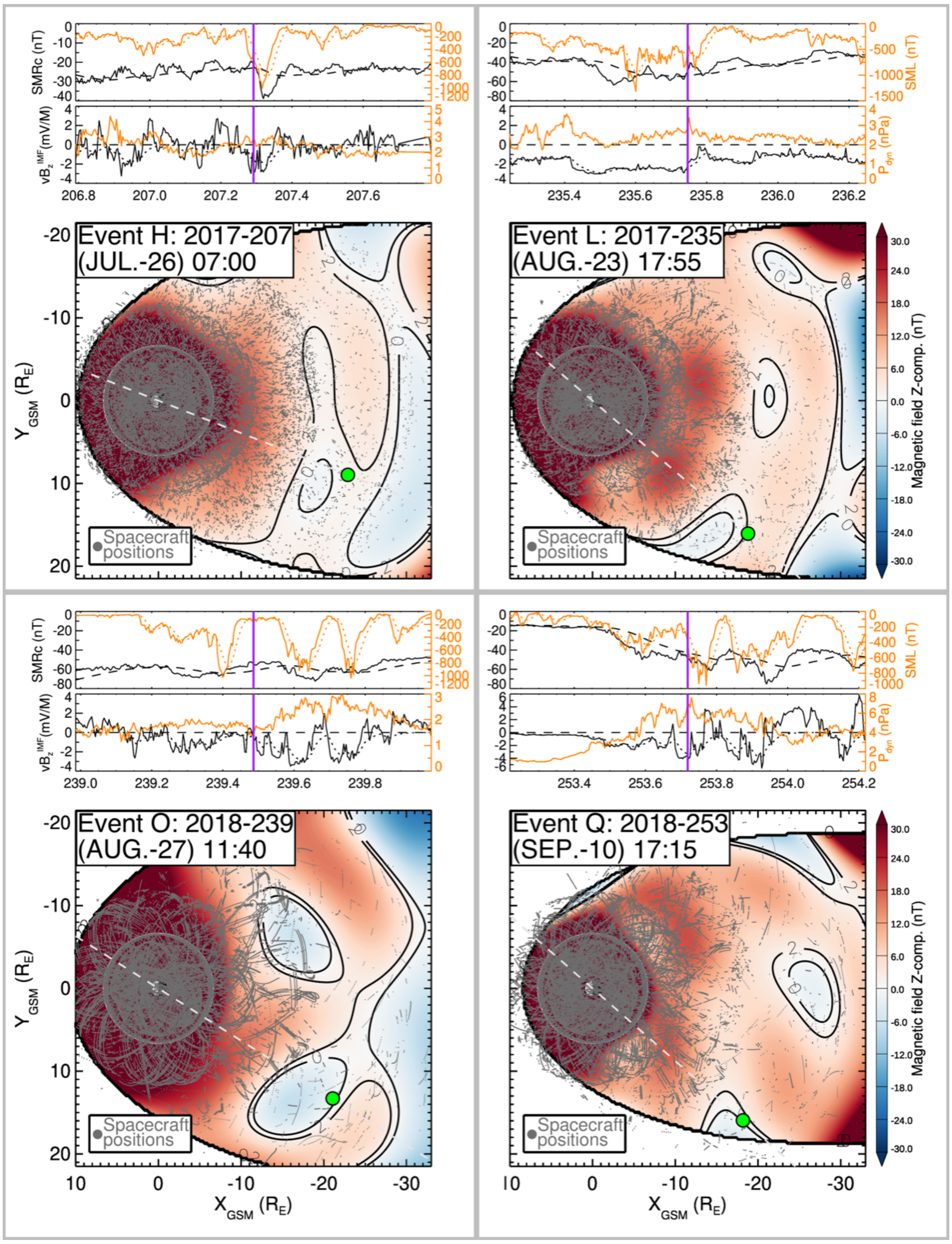

Figure S4. Ion diffusion regions and the equatorial magnetic field landscape. The format is similar to Fig. S3 except for a different group of IDR events: H, L, O, and Q. These four events are considered "hits" as the $B_z = 0$ contour is within $< 2R_E$ of the observed MMS IDR.

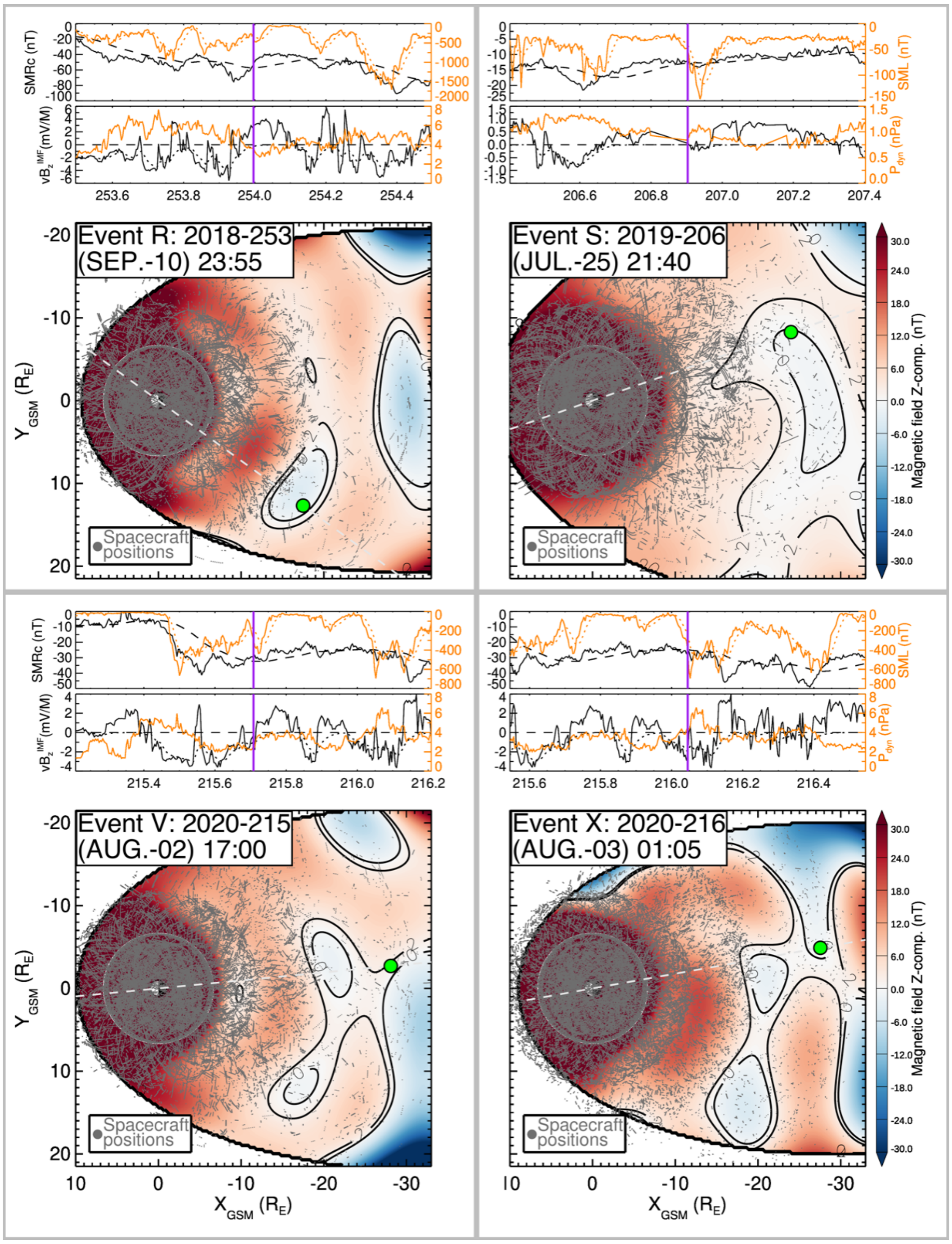

Figure S5. Ion diffusion regions and the equatorial magnetic field landscape. The format is similar to Fig. S3 except for a different group of IDR events: R, S, V, and X. These four events are considered "hits" as the $B_z = 0$ contour is within $< 2R_E$ of the observed MMS IDR.

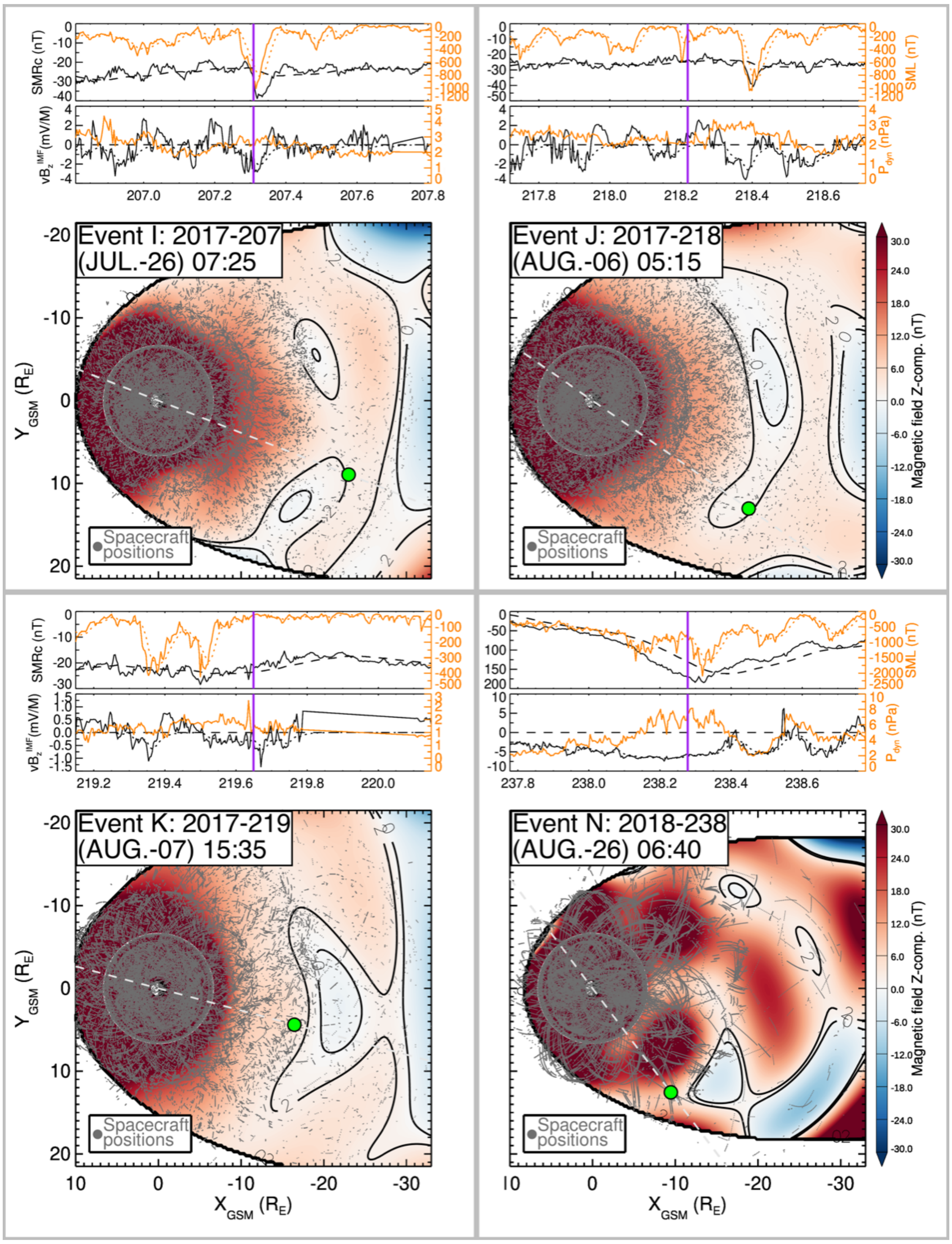

Figure S6. Ion diffusion regions and the equatorial magnetic field landscape. The format is similar to Fig. S3 except for a different group of IDR events: I, J, K, and N. These four events are not as consistent as the 16 "hits", however, the $B_z = 2$ nT is close to the observed MMS IDR for events I, J, and K and is within several R_E for of the $B_z = 0$ contour for events K and N.

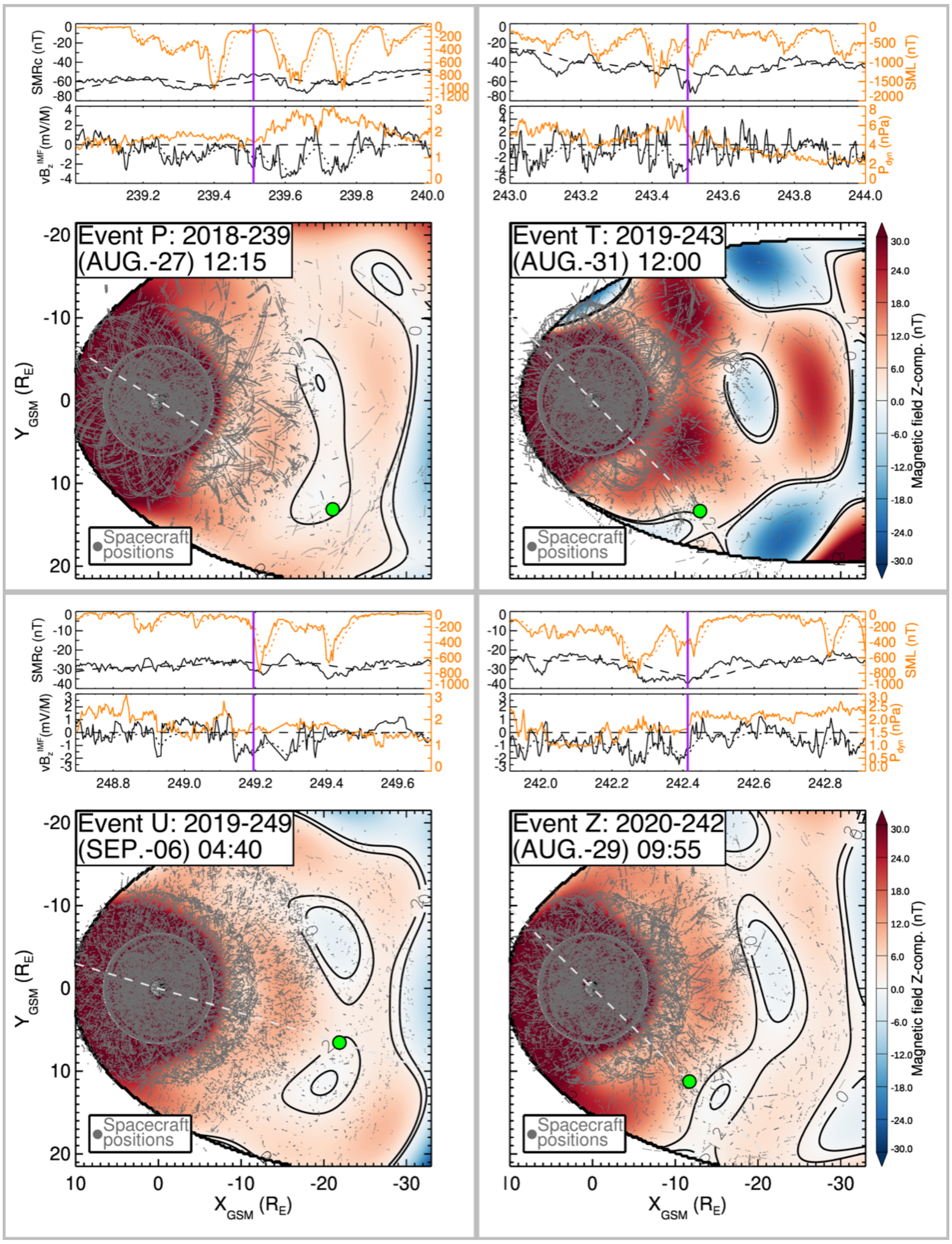

Figure S7. Ion diffusion regions and the equatorial magnetic field landscape. The format is similar to Fig. S3 except for a different group of IDR events, P, T, U, and Z. These four events are considered "near hits" as the $B_z = 2$ nT contour is within $< 2R_E$ of the observed MMS IDR.

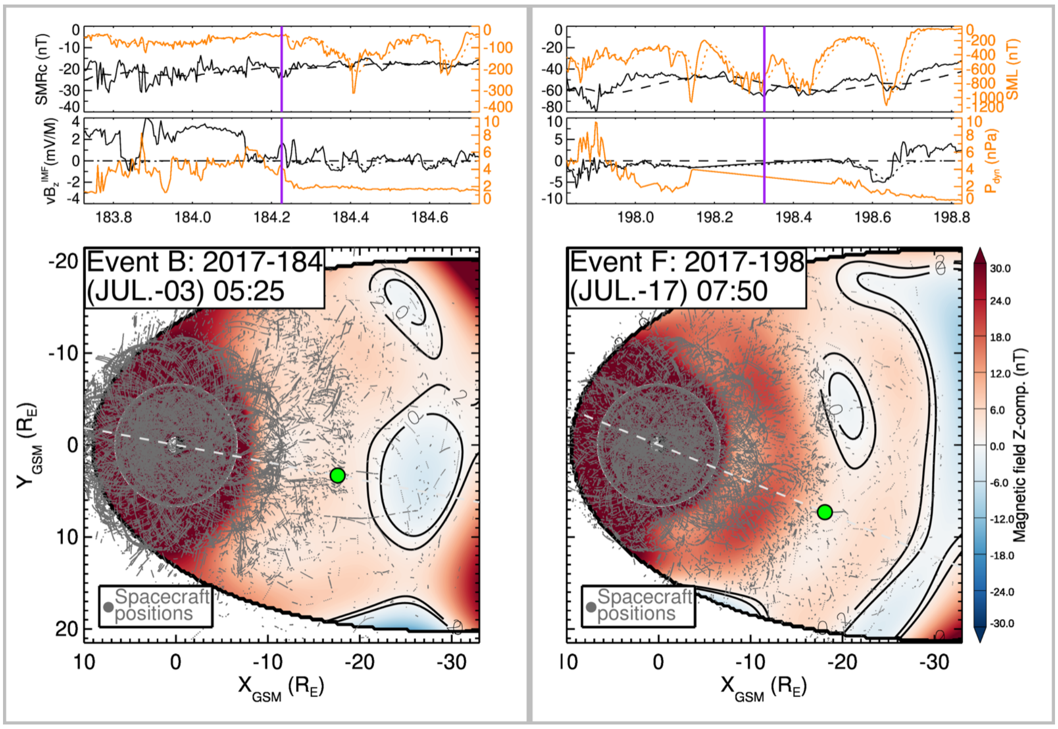

Figure S8. Ion diffusion regions and the equatorial magnetic field landscape. The format is similar to Fig. S3 except for a different group of IDR events B and F when the contours $B_z = 0$ nT and $B_z = 2$ nT are not close to the observed MMS IDR locations.

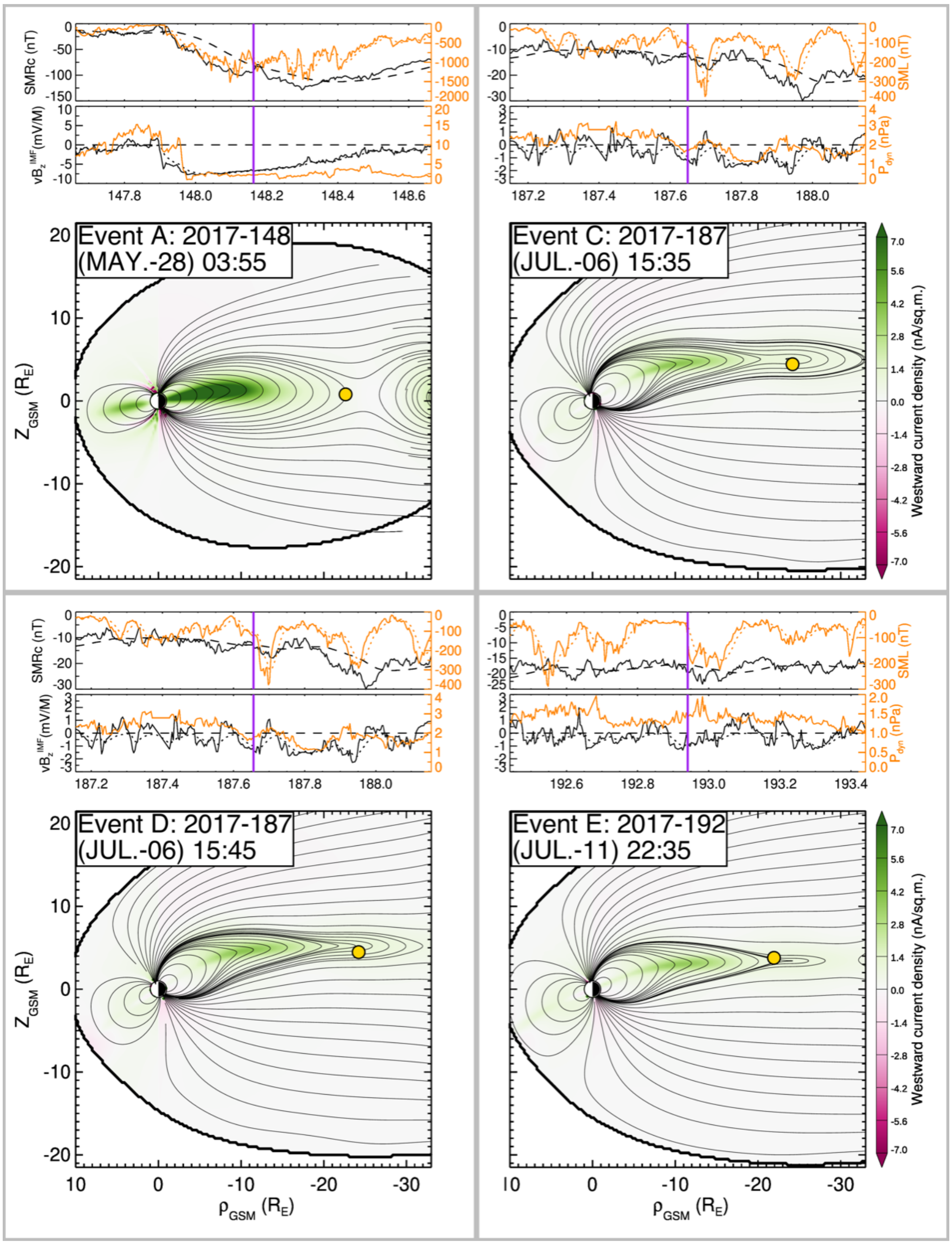

Figure S9. Ion diffusion regions against the meridional current and magnetic field distributions for events A, C, D, and E. The format is similar to Fig. 3, although the MMS IDR locations are marked by the purple dots.

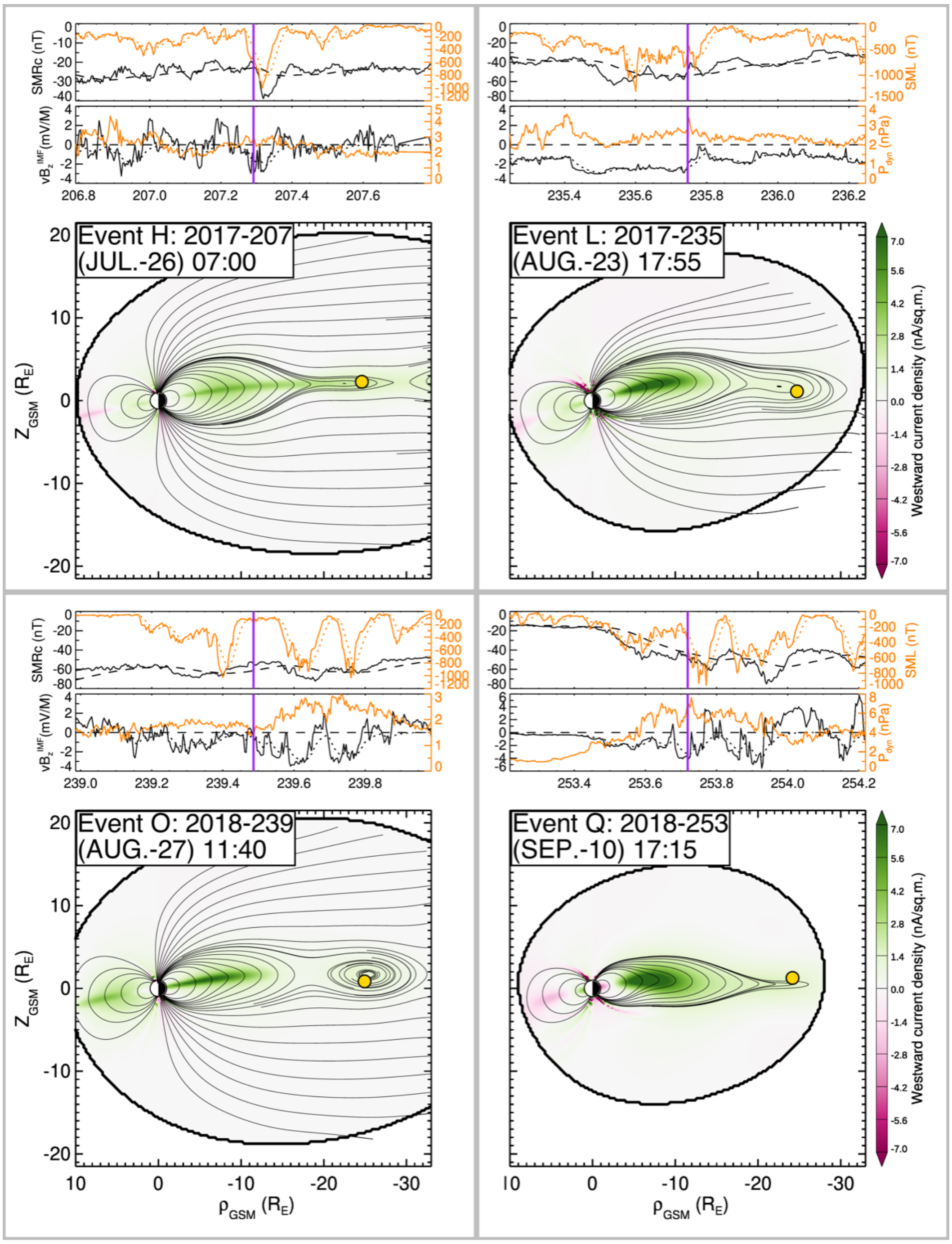

Figure S10. Ion diffusion regions against the meridional current and magnetic field distributions for events H, L, O, and Q. The format is similar to Fig. S9.

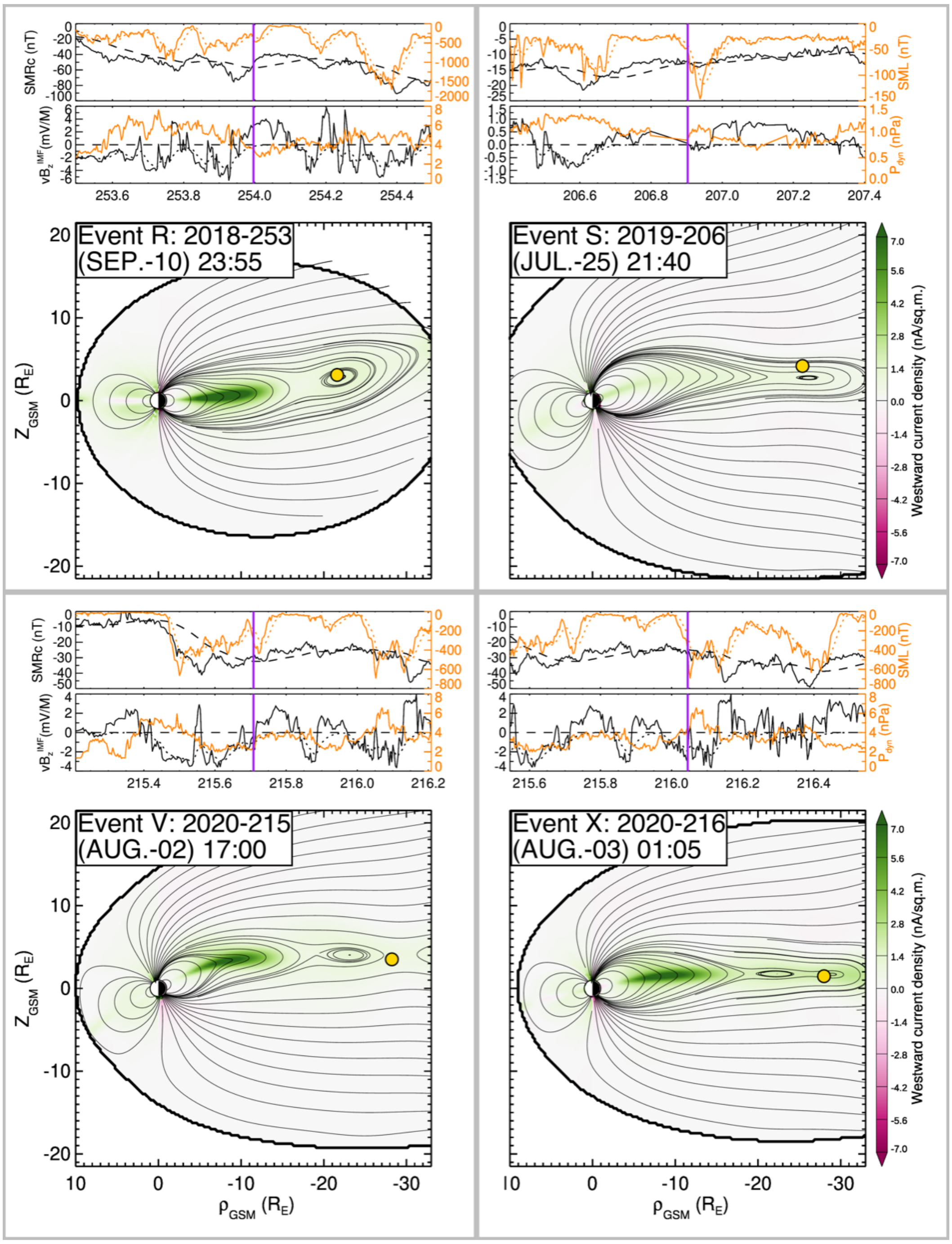

Figure S11. Ion diffusion regions against the meridional current and magnetic field distributions for events R, S, V, and X. The format is similar to Fig. S9.

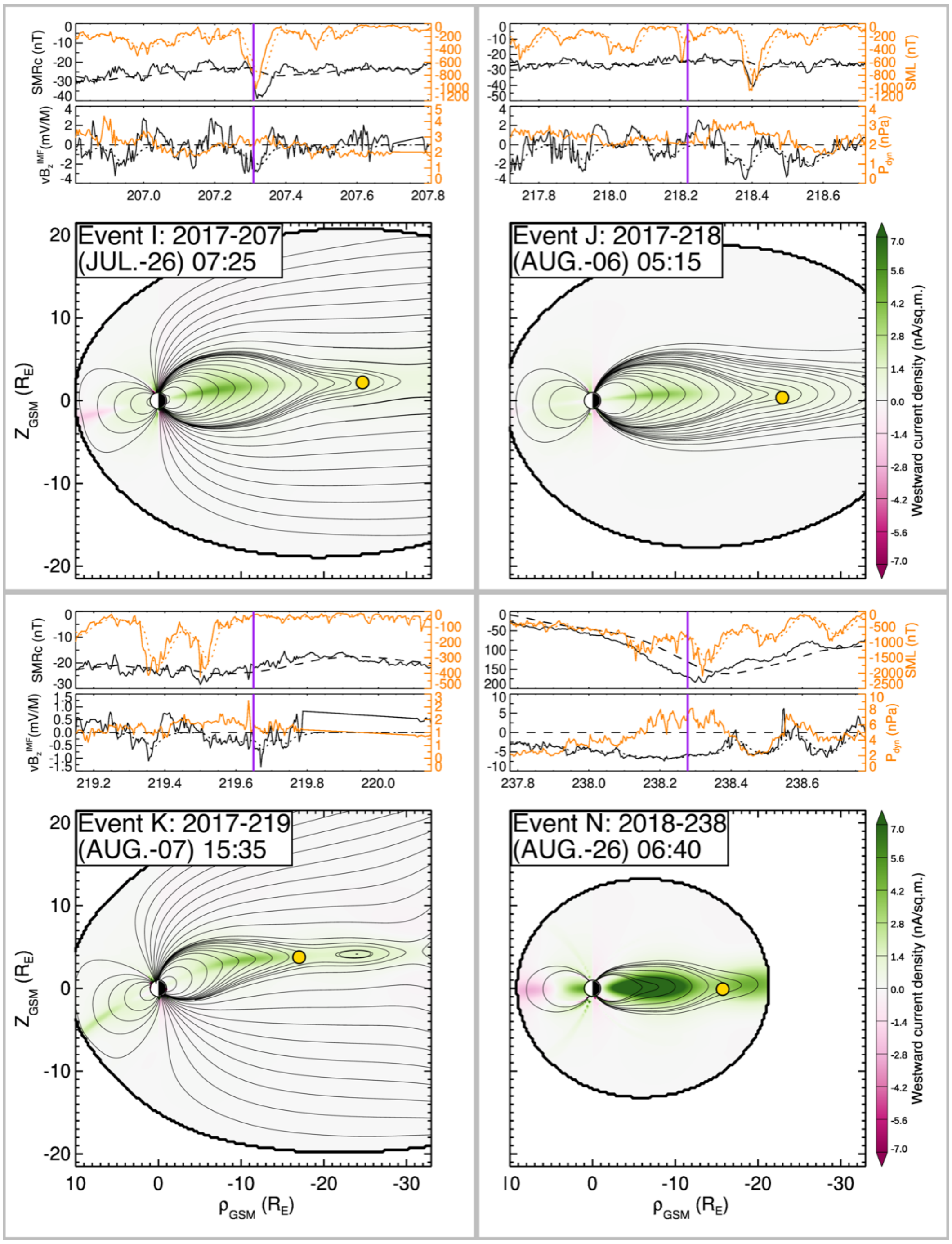

Figure S12. Ion diffusion regions against the meridional current and magnetic field distributions for events I, J, K, and N. The format is similar to Fig. S9.

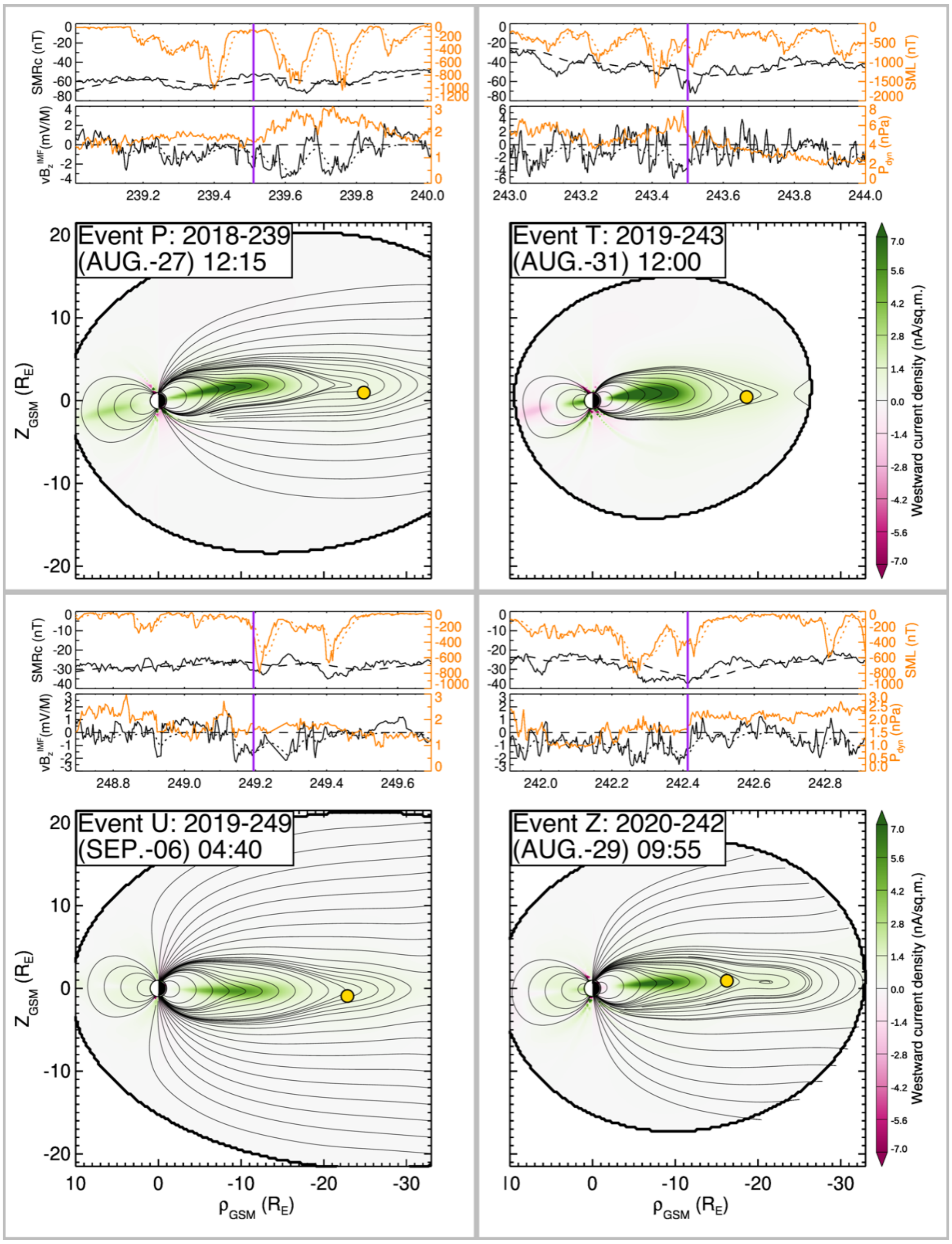

Figure S13. Ion diffusion regions against the meridional current and magnetic field distributions for events P, T, U, and Z. The format is similar to Fig. S9.

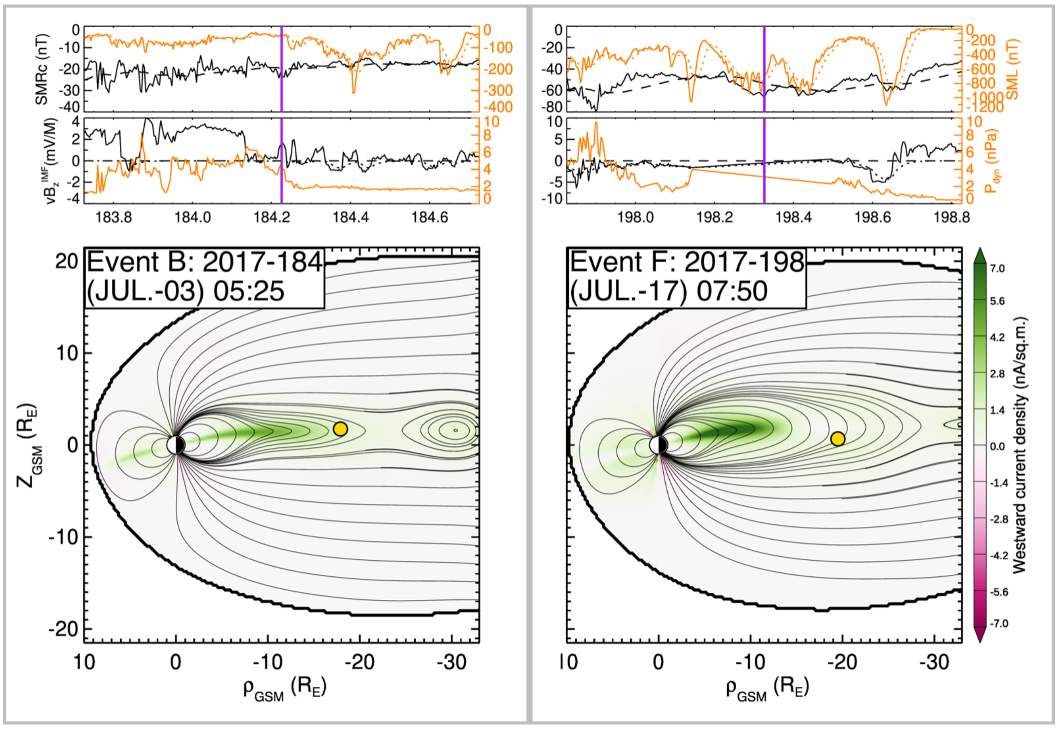

Figure S14. Ion diffusion regions against the meridional current and magnetic field distributions for events B and F. The format is similar to Fig. S9.

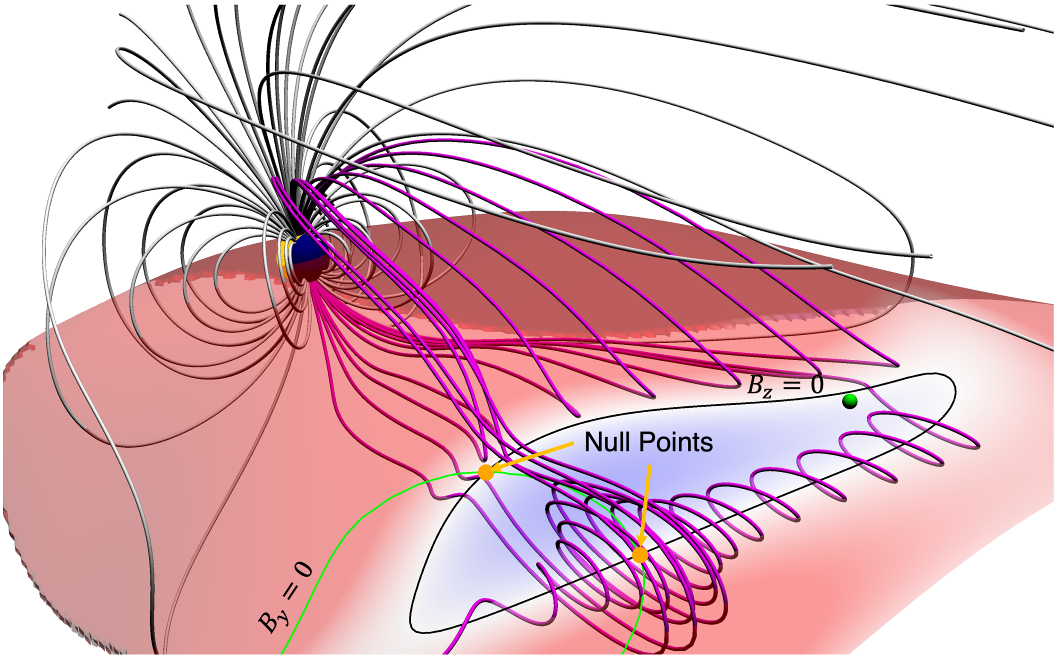

Figure S15. 3D global picture of the magnetosphere with more field lines near the expected magnetic nulls (orange tadpole marks), which are defined as intersections of the surface $B_y = 0$ with the equatorial $B_z = 0$ loop shown in Fig. 1. According to the null nomenclature (Li et al., 2021), the near-Earth and more distant null areas correspond to radial and spiral nulls.

Table S1. The Archive of Space Magnetometer Data.

Spacecraft	Number	Period	Cadence (min)
Cluster 1	756,822	2001–2015	5
Cluster 2	753,580	2001–2015	5
Cluster 3	748,084	2001–2015	5
Cluster 4	561,497	2001–2015	5
Geotail	133,107	1995–2005	15
Polar	844,212	1996–2006	5
IMP-8	10,177	1995–2000	15
GOES-8	233,674	1995–2003	15
GOES-9	84,951	1995–1998	15
GOES-10	213,295	1999–2005	15
GOES-12	79,569	2003–2005	15
THEMIS-A	702,043	2008–2015	5
THEMIS-B	78,523	2008–2011	5
THEMIS-C	115,459	2008–2011	5
THEMIS-D	702,388	2008–2015	5
THEMIS-E	711,441	2008–2015	5
Van Allen A	337,582	2012–2016	5
Van Allen B	337,610	2012–2016	5
MMS 1	312,040	2015–2020	5
MMS 2	312,050	2015–2020	5
MMS 3	311,349	2015–2020	5
MMS 4	310,219	2015–2020	5
Total	8,649,672	1995–2020	5/15

Table S2. The MMS IDR Alphabet.

Event	Start Date/Time	Model Date/Time	$D_{0nT}(R_E)$	$D_{2nT}(R_E)$	Figures
A	2017-05-28T03:57	03:55	1.94	1.40	S3 S9
B	2017-07-03T05:26	05:25	4.72	3.23	S8 S14
C	2017-07-06T15:34	15:35	0.58	3.77	S3 S9
D	2017-07-06T15:45	15:45	1.72	2.54	S3 S9
E	2017-07-11T22:33	22:35	1.37	1.46	S3 S9
F	2017-07-17T07:48	07:50	8.62	5.78	S8 S14
G	2017-07-26T00:02	00:00	1.44	1.24	F2 F3
H	2017-07-26T07:00	07:00	1.91	1.63	S4 S10
I	2017-07-26T07:27	07:25	5.18	0.39	S6 S12
J	2017-08-06T05:13	05:15	7.70	0.63	S6 S12
K	2017-08-07T15:37	15:35	3.22	1.57	S6 S12
L	2017-08-23T17:53	17:55	1.88	0.54	S4 S10
M	2018-08-15T11:57	11:55	1.47	0.70	F2 F3
N	2018-08-26T06:38	06:40	2.85	2.17	S6 S12
O	2018-08-27T11:39	11:40	0.95	1.65	S4 S10
P	2018-08-27T12:14	12:15	7.43	1.19	S7 S13
Q	2018-09-10T17:14	17:15	0.78	1.02	S4 S10
R	2018-09-10T23:57	23:55	0.88	1.64	S5 S11
S	2019-07-25T21:40	21:40	1.45	4.26	S5 S11
T	2019-08-31T12:01	12:00	1.88	0.68	S7 S13
U	2019-09-06T04:38	04:40	3.57	0.77	S7 S13
V	2020-08-02T16:58	17:00	1.06	0.61	S5 S11
W	2020-08-02T17:09	17:10	0.65	0.55	F2 F3
X	2020-08-03T01:04	01:05	1.03	2.11	S5 S11
Y	2020-08-05T14:19	14:20	1.13	3.94	F2 F3
Z	2020-08-29T09:56	09:55	3.26	1.73	S7 S13